Sparse Sampling Reconstruction of Wind Fields for Space-Borne Doppler Radars

Sparse Sampling Reconstruction of Wind Fields for Space-Borne Doppler Radars

Sérgio Luiz E. F. da Silva, Alessandro Battaglia, Cinzia Cambiotti, and Anna F. Carbone

***Abstract*—With its conically scanning W-band Doppler radar, the Wind Velocity Radar Nephoscope (WIVERN) ESA Earth Explorer 11 mission promises to provide, for the first time, global vertically resolved wind observations in cloudy and precipitating systems. Thanks to its observation geometry, WIVERN will measure line-of-sight (LoS) Doppler velocities of the same atmospheric volume from different viewing directions, allowing the complete reconstruction of the wind vector. To that end, a methodology to retrieve horizontal wind vectors for a conically scanning radar with a swath of 800 km and sparse sampling is developed in this work. The retrieval is applied to different meteorological systems, whose dynamics are simulated with a high-resolution cloud-resolving model. Results show that, in the presence of a healthy number of cloud targets in the scene, it is possible to reconstruct the zonal and meridional winds with uncertainty within 2–4 m/s. Accuracies deteriorate in the central part of the swath, close to the ground track, due to sparser sampling and interdependencies between different radar looks.**

***Index Terms*—Doppler radars, inversion analysis, remote sensing, winds.**

I. Introduction

In the last decades, remote sensing observations from satellite platforms have significantly strengthened the global observing system (GOS), initiated by the World Meteorological Organization more than 60 years ago to improve weather prediction and, subsequently, climate monitoring. Every day, millions of observations, such as temperature, pressure, wind, and relative humidity, are assimilated to feed numerical weather prediction (NWP). Among the GOS atmospheric measurements, wind field records are still incomplete (see Fig. 1), thus severely limiting modeling of NWPs and comprehensive understanding of the key processes underlying coupled climate dynamical systems.

Most direct wind observations come from radiosondes, which are daily launched from stations mainly located in the Northern Hemisphere, while very few are available over the oceans, the tropics, and the Southern Hemisphere. Surface observations are taken from land stations, ships, and buoys, and from space-borne scatterometers (indirectly derived from sea roughness recorded over the oceans). Single-level wind measurements are made from aircraft at cruising altitude and from atmospheric motion wind vectors derived from successive geostationary satellite images on top of the clouds (or from above the clouds). Aircraft also provide wind observation profiles around airports during takeoff and landing. Active instruments capable of measuring the full range of horizontal wind components (wind profilers) or line-of-sight (LoS) wind (Doppler radars and LiDARs) are available at only a few locations worldwide.

A significant advance in wind observations was achieved with the ESA Aeolus mission, launched in 2018 and completed in July 2023. Equipped with the atmospheric laser Doppler instrument (ALADIN) payload—the first space-based Doppler LiDAR [1]—Aeolus provided global profiles of LoS winds in clear sky regions and within thin clouds throughout the troposphere and lower stratosphere [2]. Note that ALADIN operates with a fixed pointing in a plane quasi-perpendicular to the flight path and 35° offset from nadir in the anti-Sun direction. ALADIN retrieves wind velocities in the range between −150 and 150 m/s at a vertical resolution of 0.25, 1, and 2 km in the planetary boundary layer (0–2 km), the troposphere (2–16 km), and lower stratosphere (16–26 km), respectively. The operational assimilation of Aeolus observations into NWP systems at various forecasting centers has demonstrated a significant positive impact on forecast accuracy (e.g., [3] and [4]).

The Wind Velocity Radar Nephoscope (WIVERN, www.wivern.polito.it, [5], [6], [7]), selected as the ESA's Earth Explorer 11 mission, is expected to fill the gap in global wind observations within storms and precipitation systems. WIVERN's unique 94-GHz conically scanning Doppler radar would provide the first space-based in-cloud wind profiles in conjunction with cloud and precipitation profile measurements. WIVERN aims to significantly improve NWP by complementing Aeolus clear-sky wind observations with in-cloud LoS wind profiles over 800-km swaths, providing near-global, quasi-daily coverage at the kilometer

Received 10 March 2026; revised 14 May 2026; accepted 26 June 2026. Date of publication 29 June 2026; date of current version 9 July 2026. This work was supported in part by Italian Space Agency (ASI) Project "Scientific studies for the Wind Velociy Radar Nephoscope (WIVERN) Mission" under Grant 2023-44-HH.0 and in part by European Space Agency under the activity "End-to-End Performance Simulator Activity of the WIVERN Mission" (ESA) under Grant 4000139446/22/NL/SD. Computational resources were provided by HPC@POLITO (http://www.hpc.polito.it). *(Sérgio Luiz E. F. da Silva, Alessandro Battaglia, Cinzia Cambiotti, and Anna F. Carbone contributed equally to this work.) (Corresponding author: Sérgio Luiz E. F. da Silva.)*

Sérgio Luiz E. F. da Silva is with the Laboratory of Parallel Architectures for Signal Processing (LAPPS), Federal University of Rio Grande do Norte, Natal, RN 59078-970, Brazil (e-mail: sergio.dasilva@polito.it).

Alessandro Battaglia is with the Department of Environment, Land and Infrastructure Engineering (DIATI), Politecnico di Turin, 10129 Turin, Italy, and also with the Department of Physics and Astronomy, University of Leicester, Leicester, U.K. (e-mail: alessandro.battaglia@polito.it).

Cinzia Cambiotti and Anna F. Carbone are with the Department of Applied Science and Technology (DISAT), Politecnico di Turin, 10129 Turin, Italy (e-mail: cinzia.cambiotti@studenti.polito.it; anna.carbone@polito.it).

Digital Object Identifier 10.1109/TGRS.2026.3708410

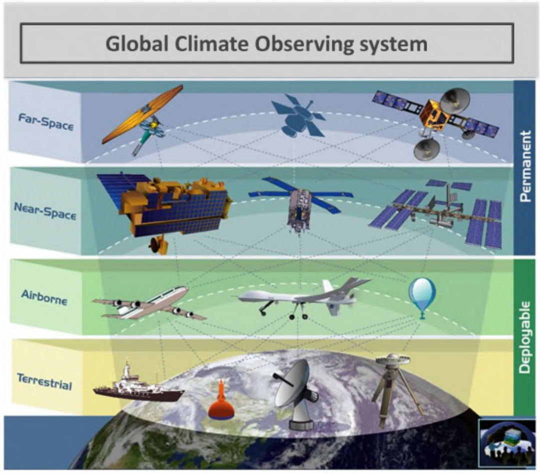

The main sources of wind measurements	Error [ms^{-1}]	Obs available for DA every 6 h	Pros & Cons
GEO VIS/IR AMV 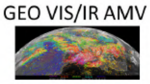	~4	≈5,000,000	Quasi global coverage at high temporal resolution; only cloud tops with uncertainties related to height
Aeolus 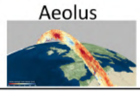	~4 or >	≈50,000	Vertical profiles in clear sky and in thin clouds. Moderate errors for Rayleigh winds, low revisit time
Aircraft 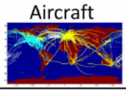	~2 or >	≈270,000	Very accurate; vertical profiles near airports; only at flight time/height on aircrafts routes
Radiosondes 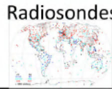	~2	≈14,000	Very accurate; vertical profiles at given location and UTC time; in decaying numbers

Fig. 1. (Left) Wind observations in the GOS are performed from a large gamut of platforms, ranging from geostationary to ground-based. The advantages and disadvantages and the average number of observations used in the Meteo-France data assimilation system and the typical errors are given in the table on the right.

scale [8], [9]. The horizontal footprint of the instrument is 0.8×1.0 km^2, with an along-range resolution of 500 m, providing a vertical resolution of circa 650 m. Hence, WIVERN would help to address fundamental weather and climate science questions by providing space observations of atmospheric dynamics and filling existing gaps within tropical cyclones [10], polar snow, and light rain observations [11], [12].

The focus of this work is to better assess the potential of WIVERN in reconstructing the vertical structure of the horizontal wind vector (i.e., the zonal and meridional components) inside weather systems in "stratiform" areas (i.e., regions with negligible convective motions). Thanks to its Doppler capability and fast movement, WIVERN can take two Doppler velocity measurements of the same targets from two different directions almost simultaneously (with a maximum separation of 2 min), enabling the wind vector to be retrieved. This is similar to what can be achieved with two ground-based Doppler radars but with two key advantages.

1) WIVERN sensitivity (single pulse sensitivity of about −18 dBZ), much higher than achievable with ground-based meteorological radars, increases the coverage to less reflective targets, particularly in the glaciated region, hence enabling the observation of divergence/convergence patterns therein.
2) The novel acquisition geometry enables the observation of winds across entire mesoscale systems spanning hundreds of kilometers within a couple of minutes.

The approach proposed here builds upon a well-established body of work on wind retrieval from multiple-Doppler radar observations. A common thread across these methods is the formulation of the retrieval as a least-squares minimization problem, in which the unknown Cartesian wind components are estimated by matching modeled LoS projections to observed Doppler velocities. Within this framework, the key differentiating factor across methods lies in the observing geometry—specifically, how azimuthal diversity is achieved. In the ground-based dual-Doppler configuration [13], two spatially separated radars provide complementary viewing angles of the same atmospheric volume, enabling decomposition of the wind vector. Airborne systems achieve a similar effect through platform motion: Guimond et al. [14] exploit the azimuth diversity and steep incidence angles of a conically scanning airborne radar with two beams (at approximately 30° and 40°), while the Electra Doppler Radar (ELDORA) [15], [16] uses fore-aft scanning to generate the necessary angular separation. In all cases, the physical constraint of mass continuity is commonly invoked to stabilize the retrieval and ensure physical consistency of the recovered wind fields. The present work extends this methodological framework to an entirely new configuration: a spaceborne W-band conically scanning Doppler radar with an 800-km swath, sparse and heterogeneous sampling, and sensitivity sufficient to detect ice-phase targets in the upper troposphere. This combination of factors—novel geometry, global scale, and cloud-resolving sensitivity—introduces challenges not encountered in ground-based or airborne contexts, motivating the multiscale constrained retrieval approach developed here.

Building on this methodological heritage, the present work contributes the following: 1) the application of a constrained least-squares wind retrieval framework to the spaceborne conically scanning geometry of the WIVERN mission—a configuration that differs fundamentally from ground-based and airborne dual-Doppler systems in terms of swath width, sampling sparseness, and azimuthal diversity—in which the anelastic mass continuity equation is incorporated as a regularization constraint with the regularization parameter selected objectively via the L-curve criterion [17]; 2) a hierarchical multiscale retrieval strategy in which the solution is progressively refined from coarse to fine spatial scales by systematically decreasing the Gaussian correlation length parameter L, mitigating instabilities associated with sparse and heterogeneous sampling while preserving dynamically relevant structures [18]; and 3) a systematic evaluation of the methodology through end-to-end simulations using high-

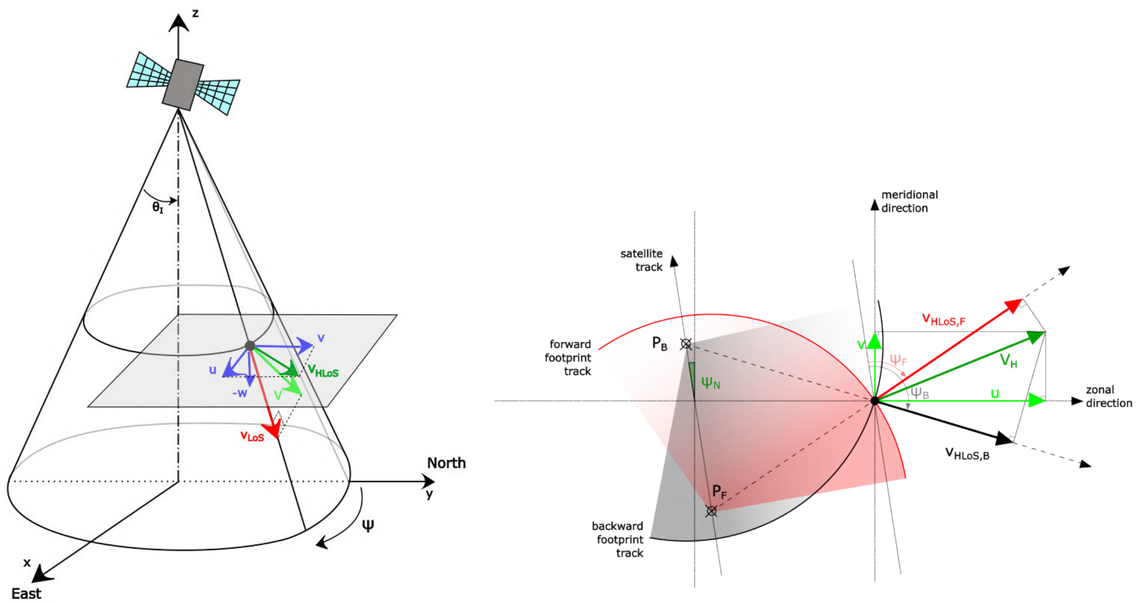

Fig. 2. Geometry of observation for the WIVERN conically scanning radar. (Left) Relationship between the WIVERN Doppler velocity measurement V_{LoS} and V_{HLoS} (the HLoS wind) in the vertical plane, including the line of sight. For better illustration, a situation with a vertical wind w is shown. (Right) Relationship between V_{HLoS} measurement and the components u and v defined in the meteorological reference frame for a forward look (subscript F) and a backward look (subscript B). This plot is drawn in the horizontal plane with the satellite in an ascending trajectory with an angle ψ_N measured clockwise from the satellite track to the North.

resolution cloud-resolving model output [19], [20] for three contrasting weather systems—a tropical cyclone, a mid-latitude Southern Ocean storm, and a high-latitude frontal system—spanning a wide range of illumination conditions, wind magnitudes, and sampling geometries, considering both noise-free and realistic noise scenarios.

The article is structured as follows. The WIVERN measurement and sampling principles are introduced in Section II. Section III describes the cloud-resolving model simulations implemented to reproduce realistic wind fields. The wind retrieval method is presented in detail in Section IV. Results are discussed in Section V, and conclusions are drawn in Section VI.

II. WIVERN Methodology of Measuring and Sampling

WIVERN's observing principle is based on the well-established Doppler radar theory signals [21], [22] with samples acquired from a fast-rotating conically scanning antenna (see Fig. 2) at different azimuth angles [6], [23].

The wind velocity can be expressed in the local meteorological system [24] as

$$\vec{V} = u\,\hat{\mathbf{x}} + v\,\hat{\mathbf{y}} + w\,\hat{\mathbf{z}} \tag{1}$$

where u is the zonal wind from west to east, v is the meridional wind from south to north, w is the vertical wind, and $\hat{\mathbf{x}}$, $\hat{\mathbf{y}}$, $\hat{\mathbf{z}}$ are the unit vectors in the W–E, S–N, and local vertical directions, respectively.

After subtracting the LoS components of the satellite velocity and of the Doppler terminal velocity of the hydrometeors (i.e., of the radar-reflectivity weighted terminal velocities of the scatterers within the backscattering volume [21]), WIVERN can estimate the LoS component of the wind, V_{LoS}, whose magnitude can be expressed as a combination of u, v, and w

$$V_{LoS} = \alpha' u + \beta' v + \gamma' w \tag{2}$$

where $\alpha' = \sin(\theta_I)\underbrace{\sin(\psi - \psi_N)}_{\alpha}$, $\beta' = \sin(\theta_I)\underbrace{\cos(\psi - \psi_N)}_{\beta}$, and $\gamma' = \cos(\theta_I)$; $\theta_I \approx 42°$ is the nadir incidence angle, and ψ (ψ_N) is the azimuth angle measured clockwise from the satellite track direction to the horizontal LoS (HLoS) direction (North direction) as illustrated in Fig. 2.

In this work, only large-scale flow horizontal winds in regions with no convective motions ($w \approx 0$) are considered. These areas will be identified by an algorithm capable of separating the stratiform versus the convective areas [25]. With such an approximation, the values of the HLoS wind velocities can be derived from the V_{LoS} measurements

$$V_{HLoS} = \frac{V_{LoS} + \left(\cancel{w} - V_T^D\right)\cos(\theta_I)}{\sin(\theta_I)} \approx \alpha\, u + \beta\, v - \frac{V_T^D}{\tan(\theta_I)} \tag{3}$$

where V_T^D is the Doppler (i.e., W-band reflectivity weighted) terminal velocity that can be estimated from empirical relationships as a function of the hydrometeor phase (solid, melting, or liquid), temperature, and attenuation-corrected reflectivity [26], [27], [28]. While, in the past, such relationships were derived from vertically pointing airborne and ground-based observations, they can now be derived globally thanks to the EarthCARE CPR measurements, whose Doppler velocities can be directly translated into a best estimate of the hydrometeors' sedimentation velocity as part of the level-2A CPR corrected Doppler data product [29]. For ice-phase particles, which dominate the glaciated regions that constitute the primary retrieval

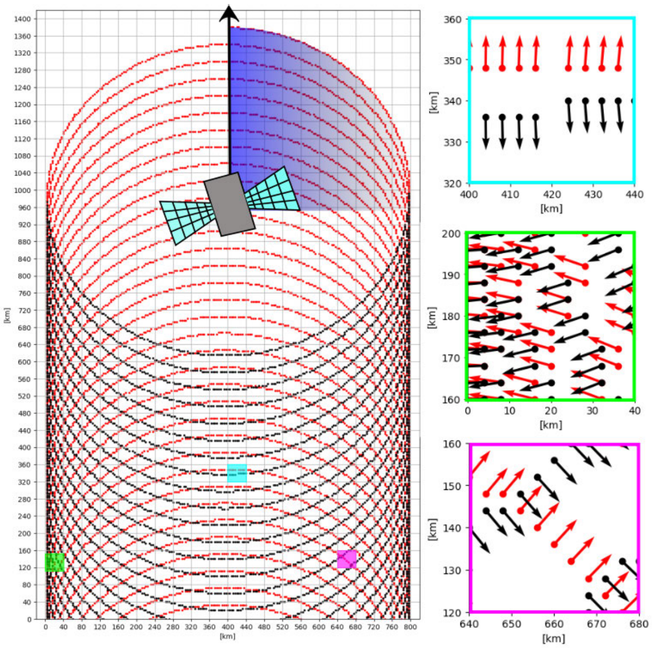

Fig. 3. Example of WIVERN scan measurements at fixed altitude. The satellite is assumed to move upward at 7.6 km/s while scanning an 800-km swath at 12 rpm. The size of the radar footprint is of the order of 1 km. Red dots correspond to forward views, and black dots correspond to backward views (forward and backward with respect to the motion of the WIVERN satellite, represented by the long black arrow). The three insets on the right show a zoom with the sampling within the three boxes highlighted in green, cyan, and pink cells, corresponding to a 40 × 40 km^2 region at the edge, center, and center of the swath. Red (black) arrows represent the HLoS wind, V_{HLoS}, for each available measurement in the cell for the forward (backward) view.

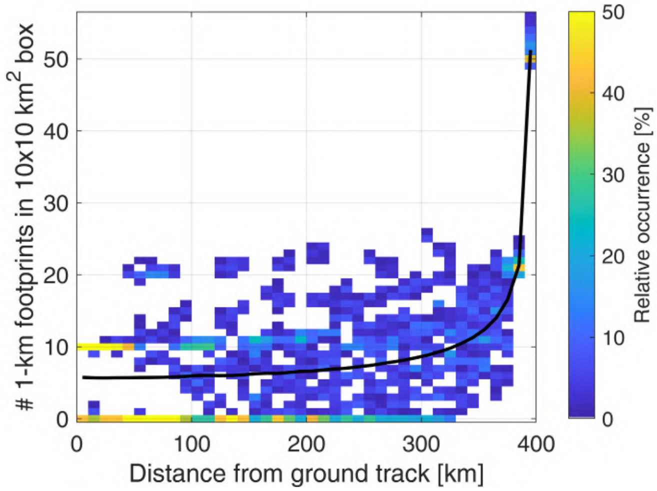

Fig. 4. Number of 1-km along-track averaged measurements in each 10 × 10 km^2 pixel for the WIVERN scanning pattern as a function of the distance from the satellite ground track. The black curve indicates the mean value, whereas the color is modulated by the relative occurrences (the sum of the relative occurrences in each column at a given distance from the ground track is 100%).

target of WIVERN in stratiform conditions, such relationships are well constrained and introduce an uncertainty of order of 0.5 m/s in V_T^D [5]. For liquid-phase hydrometeors, the spread in terminal velocity relationships is inherently larger. However, in stratiform moderate precipitation—the only regime considered here—since convective areas are explicitly screened out [25] and generally correspond to areas of strong attenuation where no WIVERN Doppler velocity measurements will be possible, rain rates are moderate, and the variability of V_T^D, due to non-Rayleigh effects remains narrow (typically between 3 and 5 m/s, [28], [30]). Near the 0 °C isotherm, where V_T^D exhibits a steep vertical gradient across the melting layer, the uncertainty is generally somewhat larger [31]; there V_T^D will be linearly interpolated between the ice and rain values. Overall, the total uncertainty budget associated with the vertical component, σ_{V_z}, which combines the uncertainty in w and in V_T^D, is set to 1 m/s in this study, consistent with the estimates provided by the WIVERN end-to-end performance studies [5]. This value is representative of stratiform conditions and is propagated into the overall $\sigma_{V_{HLoS}}$ budget discussed in Section V.

The WIVERN scan pattern is shown in Fig. 3. Dotted lines (cross-lines) correspond to the forward (backward) looks. Each measurement represents a mean value averaged over a region approximately 1 km wide (the size of the radar footprint) and of length equal to the integration length (with the WIVERN baseline product provided at 5 km). The reconstruction of the horizontal winds will be done at coarser scales for grid cells (from 1 to N_c) with resolutions of 10 or 20 km, where a total of $M^{(l)}$ fine scale measurements (with $l = 1, \ldots, N_c$) could be available. Winds are retrieved at a vertical resolution of 100m. It is clear that the coarser vertical resolution of the instrument (650 m, though samples are collected every 100m in range) makes the retrieval of winds in the presence of the strong vertical shear challenging.

Because of the scanning pattern geometry, many more measurements will be on average available in cells located at the edge rather than at the center of the swath, with a very sharp gradient in the 50 km closest to the edge (see the strong increase of the black line in Fig. 4 when approaching the swath edge). For any given distance from the ground track, the number of 1-km along-track averaged measurements in 10 × 10 km pixels is generally highly multimodal; this can be seen from the low density of colored points in Fig. 4, i.e., of points with a frequency of occurrence different from zero (white color). For instance, inside 10 × 10 km pixels just across the ground track (i.e., at 0 km distance in the x-axis), there are either no measurements (42.5% of the cases) or ten 1-km along-track averaged measurements (57.5% of the cases). The situation becomes more complicated far from the ground track with a significantly increasing percentage of pixels with no recorded data (even greater than 60%) in the first 140 km. In the two pixels closest to the sides (20-km-wide strip), a high-quality sampling is achieved with a minimum of 20 and a maximum of 56 measurements per pixel. In addition to the scanning pattern sampling, the availability of useful measurements is related to the presence of cloud targets yielding Doppler returns with high signal-to-noise ratios. Note that the measurements will have different azimuthal diversity (which is a critical feature for retrieving the u and v components) depending on their location within the swath. For example, the cyan and green cells close to the ground track of the satellite and at the edge of the swath do not exhibit much azimuthal diversity;

hence, good retrieval is expected only for the along- and cross-track components, respectively (see Fig. 3). If the satellite moves along a meridian (which is roughly the case at low latitudes, as the angle between the north and the satellite track in the ascending node is −7°), this will correspond to the meridional or zonal wind, respectively. In contrast, the red cell is characterized by looks with a wide range of azimuths, making it easier to reconstruct the full horizontal wind vector.

III. Notional Simulations

In order to study the horizontal wind inversion for realistic weather systems, the outputs of a high-resolution global model, the system for atmospheric modeling (SAM, [19], [20]), have been used. SAM has a horizontal resolution of 4.3 km and 74 vertical layers. It simulates small scales of motions coupled to large-scale circulation systems so that it explicitly resolves convection, thus overcoming the drawbacks associated with convection parameterizations [32].

Here, the output of the model for September 5, 2017, is used. The total liquid water path is shown in Fig. 5. Three precipitating systems, highlighted by three rectangles, are considered in detail in the study corresponding to: 1) Hurricane Irma over the Caribbean (Area 1); 2) mid-latitude storm in the Southern Ocean (Area 2); and 3) frontal system at very high latitudes in the Atlantic Ocean Off Labrador (Area 3). The corresponding zooms of the integrated condensed water contents together with the intensity of the horizontal winds at 5-km altitude are shown in Fig. 5 (Bottom). While the hurricane and the storm in the Southern Ocean exhibit clear cyclonic circulation around the pressure minimum, the wind field in the system off Labrador is much more complex with a strong shear region around 54° latitude.

IV. Retrieval Method for the Horizontal Wind Field

The horizontal wind velocity inversion procedure (hereinafter HWVI) entails iteratively reconstructed wind velocity fields by applying an optimization technique to match modeled data with observed data (synthetic measurements in this work). In this work, we focus on the reconstruction of zonal (u) and meridional (v) wind fields.

Considering the standard least-squares method, the HWVI can be formulated as the following optimization problem:

$$\min_{u,v} \quad \frac{1}{2}\sum_{i=1}^{N_m}(\alpha_i u+\beta_i v-(V_{HLoS})_i)^2 \tag{4}$$

where $(V_{HLoS})_i$ represents the LoS velocity measurements ($i = 1, 2, \ldots, N_m$) with N_m being the total number of radar measurements, and the linear combination $\alpha_i u + \beta_i v$ is the modeled LoS velocities (modeled data) written in terms of the unknown horizontal wind velocity components, u and v. In other words, the optimization problem presented in (4) seeks to adjust the modeled wind fields to the available observations, minimizing the error between them.

To calculate the modeled data ($\alpha_i u + \beta_i v$), the u and v wind field models are initially discretized into a mesh with several grid points. The discretization process involves dividing the spatial domain into a grid, where each point represents a specific location in the domain, as shown by the black squares in Fig. 6. At each grid point, the values of u (zonal wind component) and v (meridional wind component) are approximated. This step is indispensable because it transforms the continuous wind fields into a finite set of variables that must be handled computationally. Once the grid is defined/generated, the optimization problem is solved iteratively by finding the values of u and v that minimize the discrepancy between the modeled and observed wind velocities at each grid point. By iteratively refining the values of u and v across the grid, the values converge to the solution that best matches the observed data, ensuring an accurate reconstruction of the wind fields, as will be discussed later.

Let us consider a region with N_c grid points (the centers of which are indicated by red triangles in Fig. 6) illuminated by the radar. Since the horizontal wind vector (u_l, v_l) is the unknown in each grid point l ($l = 1, 2, \ldots, N_c$), then the minimization problem in (4) is equivalent to solving the linear system [33], [34]

$$\begin{bmatrix} \sum_{i=1}^{M^{(l)}}\alpha_i^2 & \sum_{i=1}^{M^{(l)}}\alpha_i\beta_i \\ \sum_{i=1}^{M^{(l)}}\alpha_i\beta_i & \sum_{i=1}^{M^{(l)}}\beta_i^2 \end{bmatrix}\begin{bmatrix} u_l \\ v_l \end{bmatrix} = \begin{bmatrix} \sum_{i=1}^{M^{(l)}}\alpha_i\ (V_{HLoS})_i \\ \sum_{i=1}^{M^{(l)}}\beta_i\ (V_{HLoS})_i \end{bmatrix}. \tag{5}$$

$\forall l = 1,\ 2, \ldots N_c$, which is reduced to a simple inversion for each grid point l, where $M^{(l)}$ is the number of wind velocity observations (V_{HLoS}) that are influencing or contributing to the estimation of the wind components u_l and v_l at that specific grid. It is worth noting that the value of $M^{(l)}$ varies from point to point in the grid, depending on the number of radar measurements available or relevant at each location.

A limit of this approach is the data sparseness due to the scattered nature of cloud and precipitation fields across the observation region (represented by green dots in Fig. 6). As a result, some grid boxes may lack measurements or be poorly illuminated. To address this issue, all measurements are incorporated across the entire domain ($(V_{HLoS})_i$, where $i = 1, 2, \ldots, N_m$), with each measurement weighted based on its distance from the grid point. Then, for each grid point l, the optimization problem is reformulated as follows:

$$\min_{u_l,v_l} \quad \sum_{i=1}^{N_m}\left[\xi_i^{(l)}\,(\alpha_i u_l+\beta_i v_l-(V_{HLoS})_i)\right]^2 \tag{6}$$

where $\xi_i^{(l)}$ is a weighting parameter that accounts for the relative importance of each measurement

$$\xi_i^{(l)} = \exp\left[-\left(\frac{r_i^{(l)}}{L}\right)^2\right] \tag{7}$$

with $r_i^{(l)}$ denoting the distance between measurement i and the grid point l, and $L > 0$ a scaling parameter that accounts for the correlation length of the measurements.

The quantity $\xi_i^{(l)}$ in (7) acts as a Gaussian weight, ensuring that measurements closer to the grid point contribute more significantly to the retrieval processing. Larger values of L imply that the measurements are correlated over a wider area, a

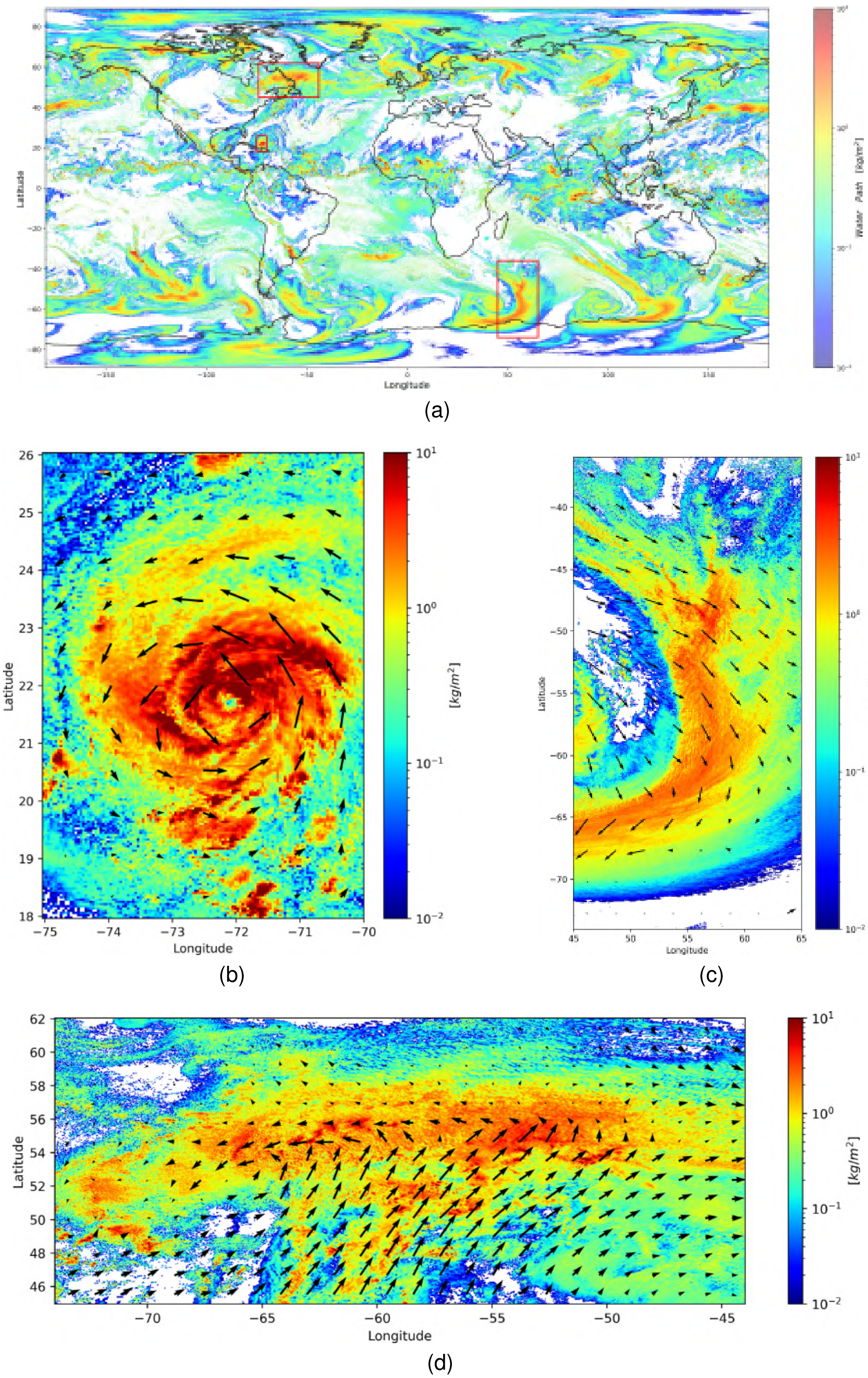

Fig. 5. (a) SAM global scene for September 5, 2017, with the total equivalent water path in kg/m^2. The three weather systems analyzed in detail are highlighted by the three rectangles. (b) Hurricane Irma over the Caribbean. (c) Mid-latitude storm in the Southern Ocean. (d) Frontal system in the Atlantic Ocean off Labrador. Black arrows correspond to the direction of the horizontal wind at 5-km altitude.

condition occurring in regions where the wind field is expected to vary smoothly. Conversely, smaller values of L indicate shorter spatial correlation, which is very likely to occur in regions with rapid variations or discontinuities in the wind

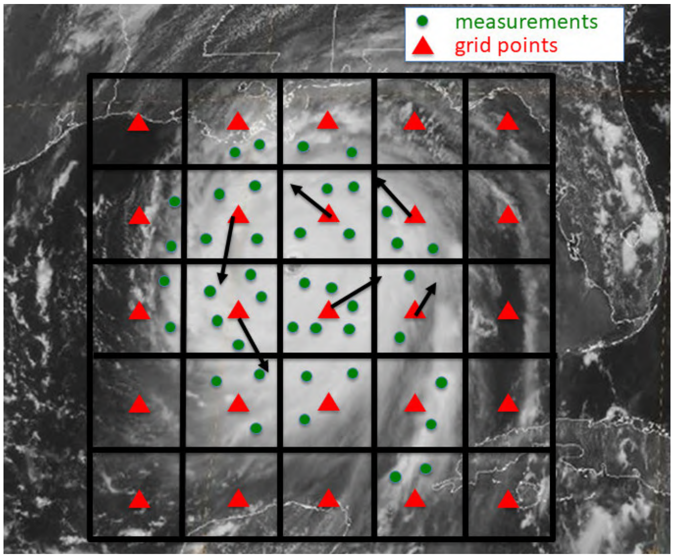

Fig. 6. Illustration of the horizontal wind velocity retrieval. The unknowns, the horizontal wind vectors (black arrows) at the center (red triangles) of each grid point (black squares), are retrieved from the sparse measurements (green dots), which correspond to the projection of the wind along the WIVERN line of sight ($V_{HLoS\ i}$).

field. In other words, the parameter L is closely tied to the correlation length of the wind field being reconstructed. When considering this approach, (5) becomes

$$\begin{bmatrix} \sum_{i=1}^{N_m} \alpha_i^2\, \xi_i^{(l)} & \sum_{i=1}^{N_m} \alpha_i\, \beta_i\, \xi_i^{(l)} \\ \sum_{i=1}^{N_m} \alpha_i\, \beta_i\, \xi_i^{(l)} & \sum_{i=1}^{N_m} \beta_i^2\, \xi_i^{(l)} \end{bmatrix} \begin{bmatrix} u_l \\ v_l \end{bmatrix} = \begin{bmatrix} \sum_{i=1}^{N_m} \alpha_i\, \xi_i^{(l)}\, (V_{HLoS})_i \\ \sum_{i=1}^{N_m} \beta_i\, \xi_i^{(l)}\, (V_{HLoS})_i \end{bmatrix} \quad \forall l = 1,\ 2, \ldots N_c. \tag{8}$$

It is worth noting that horizontal wind velocity components (u and v) could be estimated as a direct solution of the linear system defined in (8) [or (5)]. However, by doing so, the retrieved models would yield reliable estimates only in regions characterized by high or moderate radar illumination (i.e., sufficient cloud targets with radar reflectivity well above the noise level, equal to −18 dBZ for WIVERN). Hence, to retrieve physically consistent wind fields, we additionally impose a mass conservation constraint, which, for a compressible fluid, can be expressed in terms of the continuity equation as

$$\frac{\partial \rho}{\partial t} = -\nabla \cdot \left(\rho \vec{V}\right) \tag{9}$$

where ρ represents the fluid density and $\vec{V} = (u, v, w)$ denotes the velocity vector. Under the anelastic hypothesis ($|\partial\rho/\partial t| \ll |\nabla \cdot (\rho\, \vec{V})|$) and the assumption that $|\partial\rho/\partial x| \simeq |\partial\rho/\partial y| \simeq 0$, the previous relationship leads to

$$\frac{\partial u}{\partial x} + \frac{\partial v}{\partial y} = -\frac{1}{\rho}\frac{\partial(\rho\, w)}{\partial z} = -\frac{\partial w}{\partial z} - \frac{w}{\rho}\frac{\partial \rho}{\partial z}. \tag{10}$$

When the vertical wind w is negligible, the mass conservation constraint further simplifies to

$$\frac{\partial u}{\partial x} + \frac{\partial v}{\partial y} = 0 \tag{11}$$

which states that the horizontal divergence of the wind field must be zero, thereby ensuring that the mass flux is conserved in the horizontal plane. This constraint is incorporated into the least-squares problem of the u and v estimates to ensure that the reconstructed wind fields not only match the observed LoS velocities but also adhere to the fundamental physical principles governing fluid flow.

To systematically solve the least-squares minimization problem while incorporating the mass conservation constraint, we can reformulate the problem in matrix form. If we introduce the full vector of $2N_c$ unknowns, $\mathbf{x}$, defined as

$$\mathbf{x} = \left[u_1\ v_1\ u_2\ v_2\ \cdots\ u_{N_c}\ v_{N_c}\right]^T \tag{12}$$

where $(\cdot)^T$ denotes the transpose operation, and define the vector $\mathbf{b}$ with $2N_c$ elements as

$$\mathbf{b} = \begin{bmatrix} \sum_{i=1}^{N_m} \alpha_i \xi_i^{(1)}\, (V_{HLoS})_i \\ \sum_{i=1}^{N_m} \beta_i \xi_i^{(1)}\, (V_{HLoS})_i \\ \sum_{i=1}^{N_m} \alpha_i \xi_i^{(2)}\, (V_{HLoS})_i \\ \sum_{i=1}^{N_m} \beta_i \xi_i^{(2)}\, (V_{HLoS})_i \\ \vdots \\ \sum_{i=1}^{N_m} \alpha_i \xi_i^{(N_c)}\, (V_{HLoS})_i \\ \sum_{i=1}^{N_m} \beta_i \xi_i^{(N_c)}\, (V_{HLoS})_i \end{bmatrix} \tag{13}$$

then the system of equations given in (8) can be rewritten in terms of a block-diagonal matrix $\mathcal{A}$ of size $2N_c \times 2N_c$ as $\mathcal{A}\mathbf{x} = \mathbf{b}$, where $\mathbf{A}$ is a matrix that incorporates the coefficients α_i, β_i and $\xi_i^{(l)}$.

By incorporating the zero divergence condition for the horizontal wind field [mass conservation constraint; see (11)], the constrained problem can be solved by minimizing the following cost function:

$$J(\mathbf{x}) = \frac{1}{2}\|\mathcal{A}\mathbf{x} - \mathbf{b}\|_2^2 + \frac{\lambda^2}{2}\|\mathcal{D}\mathbf{x}\|_2^2 \tag{14}$$

where the first term, $1/2\|\mathcal{A}\mathbf{x} - \mathbf{b}\|_2^2$, corresponds to the least-squares data fitting (8), while the second term, $\lambda^2/2\|\mathcal{D}\mathbf{x}\|_2^2$, enforces the zero divergence constraint (11), in which $\|\cdot\|$ represents the Euclidian norm (L_2-norm) and $\mathcal{D}$ represents the discretized divergence operator. The regularization parameter λ controls the relative weight of the constraint in the optimization process, allowing for systematic balance of data fidelity and physical consistency in the solution. That is, when $\lambda = 0$, we obtain a wind field recovered exclusively through data analysis without considering the continuity equation; conversely, when $\lambda \to \infty$, the retrieved wind field strictly adheres to the continuity equation without factoring in the measurements. Hence, the selection of parameter λ is crucial to achieving a solution that effectively balances data fitting and the underlying physics.

To iteratively obtain the unknown $\mathbf{x}$, we employ a gradient-based minimization method, namely, the conjugate gradient method, to efficiently solve the optimization problem formulated in (14). In this regard, the unknown $\mathbf{x}$ is updated following [35]:

$$\mathbf{x}^{[k+1]} = \mathbf{x}^{[k]} - \gamma^{[k]} h\left(\mathbf{x}^{[k]}\right) \tag{15}$$

for $k = 0, 1, 2, \cdots, N_{iter}$, where the scalar N_{iter} is the number of iterations, $\gamma > 0$ is a step length determined via line search methods [35], h is the so-called descent direction related to the gradient of the cost function, and $\nabla J(\mathbf{x})$

$$h\left(\mathbf{x}^{[k]}\right) = \begin{cases} \nabla J\left(\mathbf{x}^{[0]}\right) & , \text{ if } k = 0 \\ \nabla J\left(\mathbf{x}^{[k]}\right) + \zeta\left(\mathbf{x}^{[k]}\right) h\left(\mathbf{x}^{[k-1]}\right) & , \text{ for } k > 0 \end{cases} \tag{16}$$

with $\mathbf{x}^{[0]}$ an initial guess (initial model) for the unknown vector and [36], [37]

$$\zeta\left(\mathbf{x}^{[k]}\right) = \frac{\nabla J\left(\mathbf{x}^{[k]}\right) \cdot \left(\nabla J\left(\mathbf{x}^{[k]}\right) - \nabla J\left(\mathbf{x}^{[k-1]}\right)\right)}{\nabla J\left(\mathbf{x}^{[k-1]}\right) \cdot \nabla J\left(\mathbf{x}^{[k-1]}\right)} \tag{17}$$

where "$\cdot$" denotes the scalar product operation. The gradient of the cost function is given by

$$\nabla J(\mathbf{x}) = \mathcal{A}^T(\mathcal{A}\mathbf{x} - \mathbf{b}) + \lambda^2 \mathcal{D}^T \mathcal{D}\mathbf{x}. \tag{18}$$

In summary, the optimization process involves iteratively determining the unknown vector $\mathbf{x}$. At each iteration, $\mathbf{x}$ is updated based on a descent direction, which is derived from the gradient of the cost function. This process starts with an initial model ($\mathbf{x}^{[0]}$) and refines it step by step to minimize the cost function. In Sections IV-A–IV-C, we will discuss how to obtain the initial model ($\mathbf{x}^{[0]}$) and the regularization parameter (λ). In addition, let us remind readers that we perform this optimization multiple times, each associated with a different scale, following a multiscale approach. Each scale corresponds to a specific L-value, which is related to the resolutions of the retrieved models, as will be discussed later.

A. First Guess Wind Field (Initial Model)

To obtain an initial model $\mathbf{x}^{[0]}$, we adopt a two-step process. The first step involves directly solving the regularized least-squares problem formulated in (14), while the second step incorporates an interpolation condition into the model recovery process. In particular, in the *first step*, note that the cost function in (14) can be equivalently reformulated as an ordinary regularized least-squares problem, expressed as follows:

$$\min_{\mathbf{x}} \quad J(\mathbf{x}) = \frac{1}{2}\left\| \begin{pmatrix} \mathcal{A} \\ \lambda\mathcal{D} \end{pmatrix} \mathbf{x} - \begin{pmatrix} \mathbf{b} \\ \mathbf{0} \end{pmatrix} \right\|_2^2. \tag{19}$$

Given that the columns of matrix $\mathcal{A}_\lambda = [\mathcal{A}^T, \lambda\mathcal{D}^T]^T$ are linearly independent, it follows that the matrix $\mathcal{A}_\lambda^T \mathcal{A}_\lambda$ is positive definite. This implies that the cost function J is strictly convex, and as a result, the regularized least-squares problem described in (19) has a unique solution [38] given by

$$\mathbf{x}^{[0]} = \left[\left(\mathcal{A}^T\mathcal{A} + \lambda^2\mathcal{D}^T\mathcal{D}\right)^T \left(\mathcal{A}^T\mathcal{A} + \lambda^2\mathcal{D}^T\mathcal{D}\right)\right]^{-1} \mathcal{A}^T \mathbf{b}. \tag{20}$$

In this work, we compute the inverse matrix of the expression enclosed in brackets in (20) using the Moore–Penrose pseudoinverse due to its robustness to deal with ill-conditioned or singular linear systems while maintaining numerical stability [39].

In the *second step*, we perform an interpolation process to address the sparse sampling of the WIVERN mission. Such interpolation is applied only to grid points with low illumination, specifically targeting locations where the number of available measurements is insufficient or nonexistent. The identification of low-illumination areas is guided by an illumination map $\mathcal{I}_L$, which is determined by the positions of radar wind measurements. The illumination in each cell is defined by summing all the weights $\xi_i^{(l)}$ in (7) at each grid point, i.e.,

$$\mathcal{I}_L^{(l)} \equiv \sum_{i=1}^{N_m} \xi_i^{(l)} = \sum_{i=1}^{N_m} \exp\left[-\left(\frac{r_i^{(l)}}{L}\right)^2\right] \tag{21}$$

where the summation extends over all measurements in the domain.

Furthermore, to characterize the overall observational coverage of a given scene, we define the domain-averaged illumination parameter

$$\bar{\mathcal{I}}_L = \left\langle \mathcal{I}_L^{(l)} \right\rangle_{scene} = \frac{\sum_{l=1}^{N_c} \mathcal{I}_L^{(l)}}{N_c} \tag{22}$$

where $\langle \cdot \rangle$ denotes the areal mean over all N_c grid points. The averaged illumination indicates how well the entire observation region is illuminated by the available measurements. A higher value of $\mathcal{I}_L$ indicates denser observational coverage, while lower values suggest regions with very sparse or insufficient sampling.

In this way, regions of the initial model reconstructed in the first step and associated with a pixel illumination (21) below a cutoff will be identified as having low illumination and reset to a "Not a Number" (NaN) element. Then, they are replaced with elements determined using an interpolation function $f(\mathbf{y}^0)$, where $\mathbf{y}^0$ represents the subset of non-NaN elements in $\mathbf{x}^{[0]}$. Given the illumination map $\mathcal{I}_L$ associated with the radar acquisition geometry and a cutoff value $\mathcal{I}_{\text{cutoff}}$, we define this step as

$$x_l^0 = \begin{cases} x_l^0 & , \quad \text{if } \mathcal{I}_L^{(l)} \le \mathcal{I}_{\text{cutoff}} \\ f\left(\mathbf{y}^0\right), & \quad \text{otherwise} \end{cases} \tag{23}$$

where x_l^0 is the lth element of $\mathbf{x}^{[0]} = (x_1^{[0]}, x_2^{[0]}, \ldots, x_{2N_c}^{[0]})$.

In this work, we use a scattered data interpolation method to perform interpolation and replace NaN values. This method constructs an interpolation function based on known data points and their associated values and utilizes Delaunay triangulation [40], which generates a mesh of triangles from the known (non-NaN) points. Next, we evaluate the interpolation function at NaN points using the natural-neighbor interpolation method [41], which estimates the value of a NaN point by weighting the values of the nearest known (non-NaN) points. This weighting is based on the areas of the cells formed by the triangulation. This promotes smoothness and continuity in the initial model while minimizing unwanted artifacts [42].

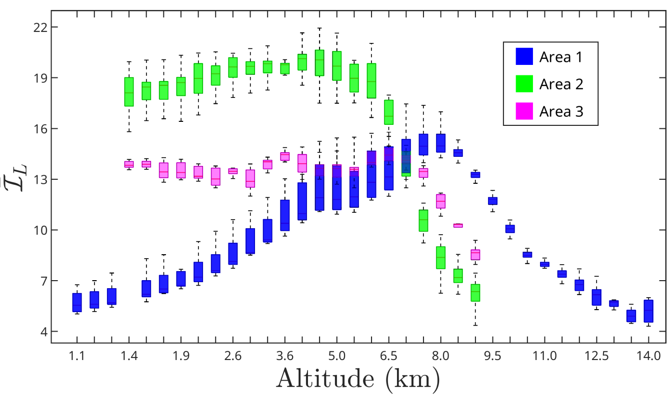

Fig. 7. Boxplots of the mean illumination distribution, as defined by (22), for $L = 40$ km, corresponding to cross sections at different altitudes for Area 1 (blue lines), Area 2 (green lines), and Area 3 (pink lines). Each boxplot is constructed from nine, ten, and five ascending passes, along with an equal number of descending passes, for Areas 1, 2, and 3, respectively. The center red line represents the median of the illumination map; the box represents the IQR, with in the bottom of the box the first quartile (Q_1, or 25% of the mean illumination values) and in the top the third quartile (Q_3, or 75% of the mean illumination values). The whiskers extend to values that are not considered outliers (they extend up to 1.5 times the IQR from the quartiles).

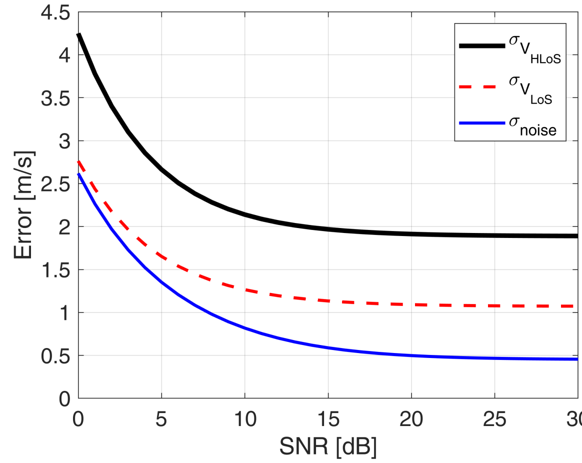

Fig. 8. Error expected for the WIVERN radar wind measurements when averaged over a 5-km along-scan integration length as a function of the SNR for the LoS wind (red dashed line) and the HLoS (black thick line). The noise error only due to the radar Doppler estimates [see (26)] is plotted in the blue line. For the expected WIVERN performance, SNR = 0 dB corresponds to a radar reflectivity of −18 dBZ.

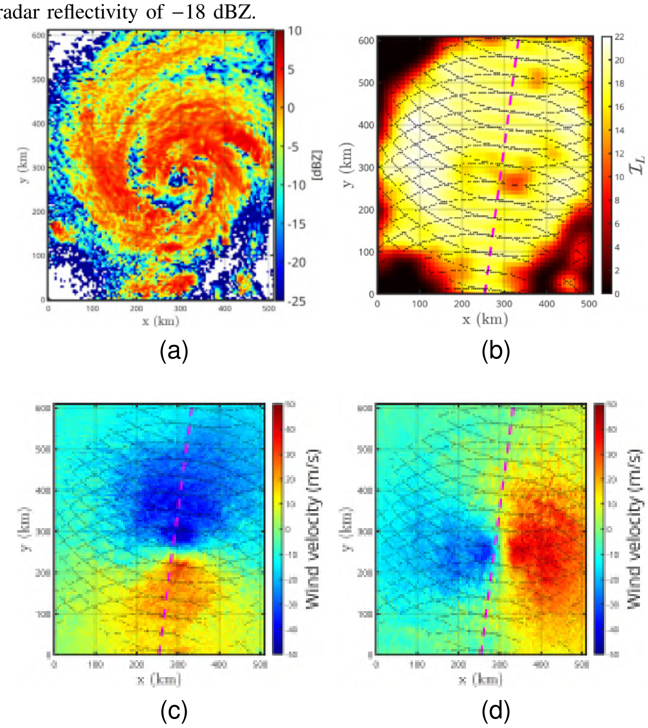

Fig. 9. Simulation of a WIVERN overpass of the Hurricane Irma weather system for a descending orbit passing close to the eye of the hurricane. A cross section at an altitude of 7 km is shown. The retrieval is performed on grid boxes with a size of 10×10 km^2. (a) 94-GHz measured reflectivity (accounting for the slant-view attenuation). (b) Illumination $\mathcal{I}_L$ with $L = 40$ km as provided by (21), where values close to light colors correspond to high illumination (densely sampled points) and dark colors denote low illumination (dispersed sampled points), with black indicating the absence of valuable information. (c) and (d) Model zonal (u) and meridional (v) winds used as the ground truth. The black dots represent radar-sampled points with reflectivity above the radar sensitivity, while the pink line indicates the satellite ground track.

B. Selection of Regularization Parameter

Selecting an appropriate regularization parameter is a critical step for controlling the tradeoff between the measurement and physics terms, preventing overfitting, and mitigating numerical instabilities. An inadequate choice of λ may lead to either overfitting sparse observations or excessive smoothing of dynamically relevant structures, and it may also affect the numerical conditioning of the inverse problem [43]. To address this, we consider the L-curve criterion [17], a well-established technique widely used in the literature for regularization parameter selection [44], [45]. The L-curve provides a compact diagnostic of the tradeoff between the data misfit $(1/2\|\mathcal{A}\mathbf{x} - \mathbf{b}\|_2^2)$ and regularization $(1/2\|\mathcal{D}\mathbf{x}\|_2^2)$ terms by plotting their norms in log–log space. The characteristic “L” shape arises from the competing effects of data fitting and physical smoothing, and the vicinity of the curve’s corner identifies a regime in which both requirements are simultaneously satisfied [46].

To construct the L-curve, we first define a set of candidate values for λ, from $\lambda_{\min}$ to $\lambda_{\max}$. For each value of λ, we solve the regularized inverse problem given by (19) to obtain the estimated solution $\hat{\mathbf{x}}_\lambda$. Using this solution, we compute the data misfit term $1/2\|\mathcal{A}\hat{\mathbf{x}}_\lambda - \mathbf{b}\|_2^2$ and the regularization term $1/2\|\mathcal{D}\hat{\mathbf{x}}_\lambda\|_2^2$. These quantities are then plotted against each other on a logarithmic scale to form the L-curve. Once we have constructed the L-curve, we determine the optimal regularization parameter $\hat{\lambda}$ as the point that minimizes the Euclidean distance to the origin in log–log space, i.e.,

$$\hat{\lambda} = \underbrace{\operatorname{argmin}}_{\lambda\in[\lambda_{\min},\, \lambda_{\max}]} \sqrt{\left[\log\left(\frac{1}{2}\|\mathcal{A}\hat{\mathbf{x}}_\lambda - \mathbf{b}\|_2^2\right)\right]^2 + \left[\log\left(\frac{1}{2}\|\mathcal{D}\hat{\mathbf{x}}_\lambda\|_2^2\right)\right]^2}. \tag{24}$$

It is worth emphasizing that this criterion identifies the solution that achieves the most favorable compromise between data fidelity and physical consistency, without relying on subjective tuning [43].

C. Multiscale Approach

The L-parameter defines the spatial resolution at which the wind velocity is reconstructed: a large L yields a smoother

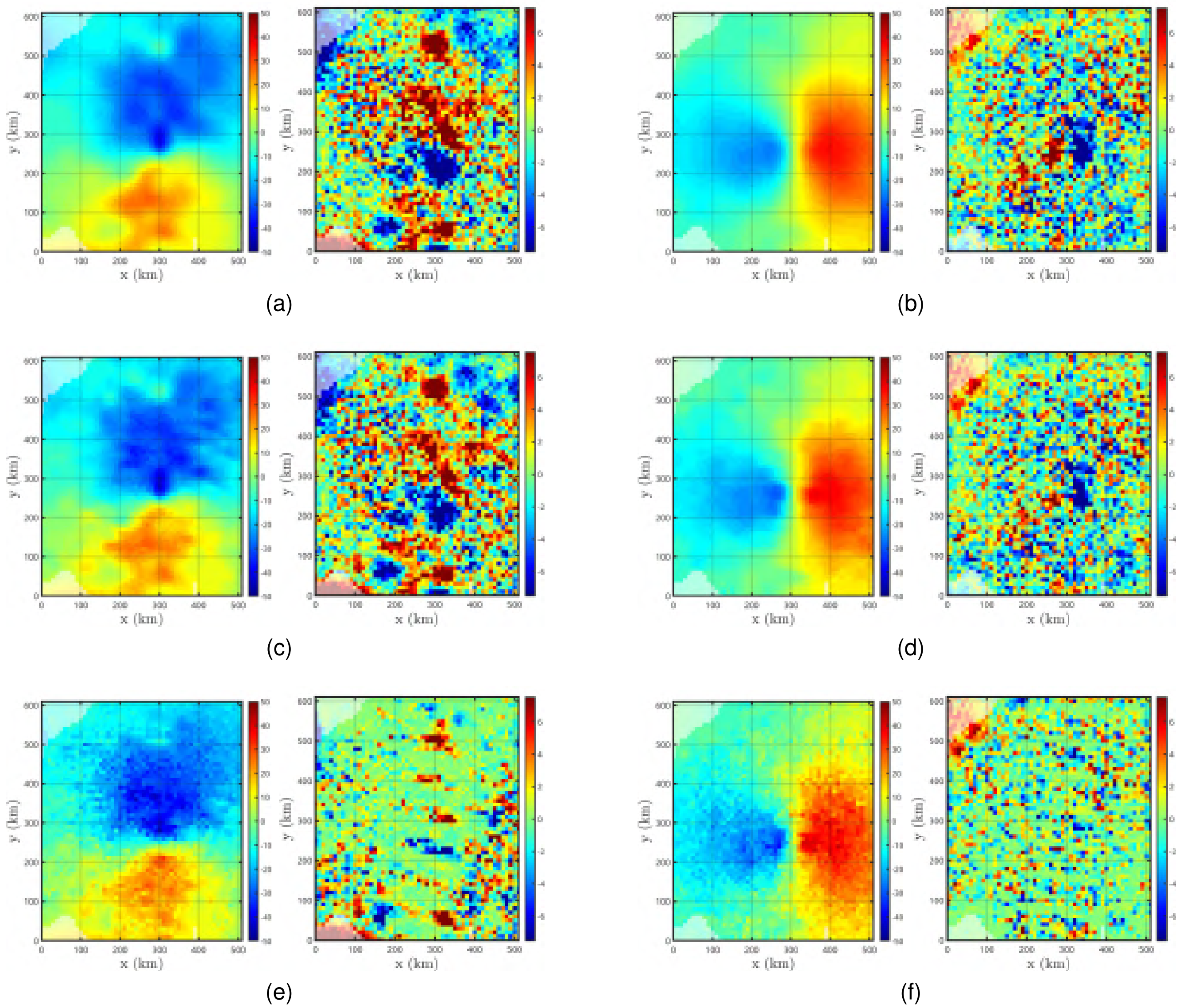

Fig. 10. Retrievals of the horizontal wind for the scene shown in Fig. 9 for different iteration steps of the procedure described in Section IV. The first column [(a)-(c)-(e)] illustrates results for the zonal wind (u), whereas the second column [(b)-(d)-(f)] shows the meridional wind (v). (a) and (b) First guess of u and v, respectively, obtained from the solution of (20) with the corresponding errors computed with respect to the model reference fields depicted in Fig. 9(c) and (d). (c) and (d) Retrieved solution at an intermediate step of the multiscale approach, with L = 15 km. (e) and (f) Final retrieved models with L = 10 km after the complete multiscale processing. Grid points with illumination $\mathcal{I}_L^{(l)} < 0.5$ which have been shaded.

solution, effectively filtering out small scales and irregularities caused by sparse sampling. In contrast, a small L results in a more localized weighting, with only nearby observations influencing the inversion at each grid point.

In this context, we propose a multiscale inversion approach as follows: starting from an initial guess, the solution is progressively refined by systematically decreasing the correlation length parameter L. The algorithm starts with a large L, which ensures a smooth and well-regularized initial estimate and then gradually decreases L to introduce finer-scale structures while maintaining stability throughout the inversion process.

By structuring the inversion in this way, we leverage the large-scale coherence of the initial solution while gradually incorporating smaller-scale features in a controlled manner, thereby obtaining high-resolution models. Furthermore, the multiscale approach avoids common pitfalls associated with single-scale inversions, such as sensitivity to noise when using small L or excessive smoothing when using large L throughout the entire process [18], [47].

V. Numerical Experiments

In this section, we first demonstrate the potentialities of the multiscale continuity-constrained least-squares methodology for retrieving horizontal wind fields within dynamic weather systems from the sparse sampling envisaged for the WIVERN mission. The selection of the regularization parameter controlling the relative weight of the mass-conservation constraint is performed objectively using the L-curve criterion; details and sensitivity analyses are provided in Section IV-B and the Appendix.

The first step in our analysis is to define the specific regions to be examined. Within these regions, we identify

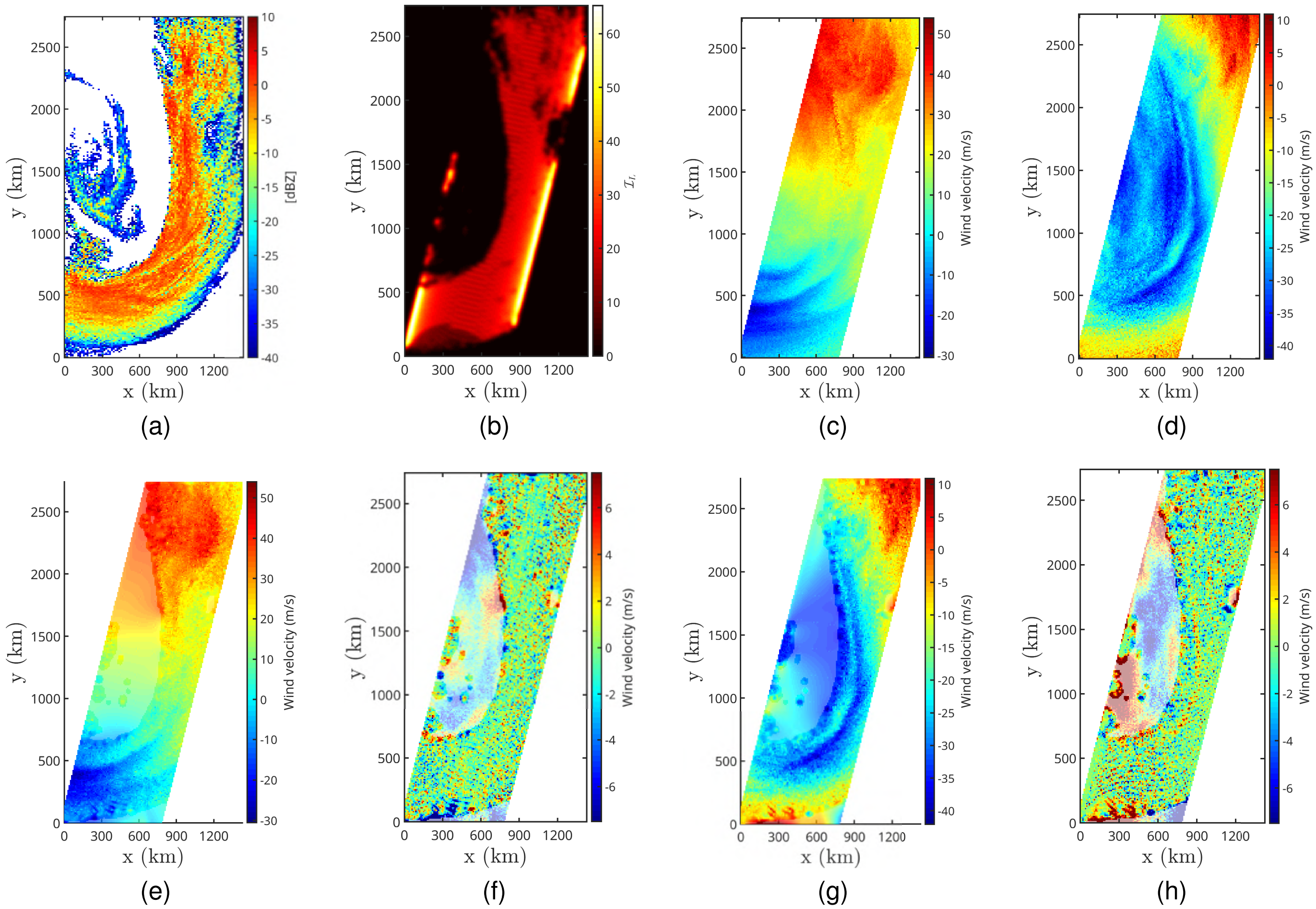

Fig. 11. Simulation of a WIVERN overpass of the mid-latitude storm in the southern ocean (Area 2). A cross section at an altitude of 4.5 km is shown. (a) 94-GHz measured reflectivity (accounting for the slant-view attenuation). (b) Illumination $\mathcal{I}_L$ (21) with $L = 40$ km; the mean illumination $(\bar{\mathcal{I}}_L)$ is 21.16. (c) and (d) Model zonal (u) and meridional (v) winds used as the ground truth. (e) and (g) Final retrieved models after the complete downscaling processing. (f) and (h) Corresponding errors computed with respect to the model reference fields depicted in (c) and (d). In the bottom figures, grid points with illumination $\mathcal{I}_L^{(l)} < 0.5$ have been shaded.

radar-illuminated areas and extract the associated measurements. Once the dataset was selected, we obtained the mean illumination $(\bar{\mathcal{I}}_L)$ distributions for each area and selected altitude using (22). Fig. 7 shows boxplots of the mean illumination distribution, for $L = 40$ km, corresponding to cross sections at different altitudes for Area 1 (blue lines), Area 2 (green line), and Area 3 (pink line). In each boxplot, the central red line represents the median of the mean illumination distribution at a given altitude. The interquartile range (IQR) is indicated by the box, where the lower boundary corresponds to the first quartile (Q_1, the 25th percentile), and the upper boundary represents the third quartile (Q_3, the 75th percentile). The whiskers extend to the largest and smallest values that are not considered outliers, with lengths limited to 1.5 times the IQR between the quartiles. We observe a clear variation in mean illumination levels across different altitude ranges in each study area. In Area 1 (blue line), the median illumination increases with altitude, reaching a peak before decreasing at higher altitudes. This is due to strong attenuation caused by liquid precipitation below the freezing level in the hurricane, which drives the signal below the detection threshold and, thus, reduces illumination. On the other hand, illumination remains above 4 up to 14 km, due to the presence of ice clouds with significant water contents up to such altitudes. A different behavior is observed in the other two areas (green and pink lines) with the maximum illumination encountered in the first 6/7 km and then dropping rapidly above 7 km.

End-to-end simulations of WIVERN radar signals have been studied in detail in recent years (e.g., [23]). Besides accounting for the WIVERN geometry, they account for the noisiness of the pulse-pair estimator [22], presence of clutter (see [12]), nonuniform beam filling, and wind shear errors (see [48]). A detailed analysis of the errors associated with the Doppler velocities has been conducted in preparation for the user consultation meeting (see [5]). The standard deviation of the HLoS Doppler velocities, $\sigma_{V_{HLoS}}$ (black thick continuous line in Fig. 8), is the result of the uncertainty on the LoS wind ($\sigma_{V_{LoS}}$, red dashed line in Fig. 8) and of the uncertainty associated with the vertical component motion $(w - V_T^D)$ here indicated with σ_{V_z}). It can be computed as

$$\sigma_{V_{HLoS}} = \sqrt{\left(\frac{\sigma_{V_{LoS}}}{\sin\theta_I}\right)^2 + \left(\frac{\sigma_{V_z}}{\tan\theta_I}\right)^2}. \quad (25)$$

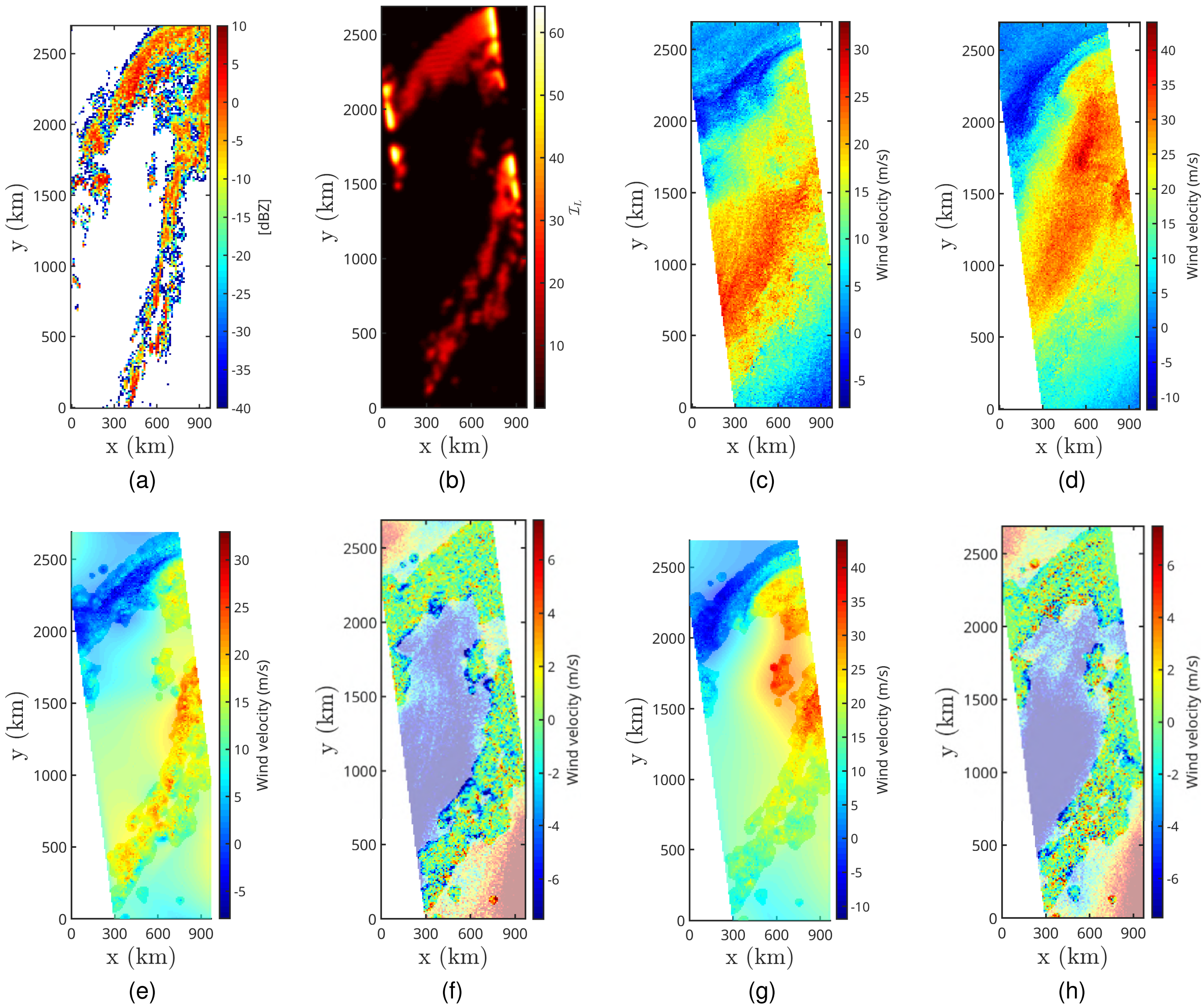

Fig. 12. Simulation of a WIVERN overpass of a frontal system in the Atlantic Ocean Off Labrador, referred to here as Area 3. A cross section at an altitude of 5 km is shown. (a) 94-GHz measured reflectivity (accounting for the slant-view attenuation). (b) Illumination $\mathcal{I}_L$ (21) with $L = 40$ km; the mean illumination ($\bar{\mathcal{I}}_L$) is 14.11. (c) and (d) Model zonal (u) and meridional (v) winds used as the ground truth. (e) and (g) Final retrieved models after the complete multiscale processing. (f) and (h) Corresponding errors computed with respect to the model reference fields depicted in (c) and (d). In the bottom figures, grid points with illumination $\mathcal{I}_L^{(l)} < 0.5$ have been shaded.

σ_{V_z} is the result of the uncertainty in w (estimated to be 0.7 m/s in stratiform regions) and of the error in the estimation of V_T^D (see Section II), for a total uncertainty of 1 m/s.

On the other hand, $\sigma_{V_{LoS}} = (\sigma_{noise}^2 + \sigma_{nubf}^2)^{1/2}$ where the first component is the uncertainty associated with the noisiness of the radar measurements [22] (blue continuous line in Fig. 8), and the second term, σ_{nubf}, accounts for a random error introduced by nonuniform beam filling effects and is estimated to be of the order of 1 m/s [23]. The noise error is a strong function of the signal-to-noise ratio (SNR) of the signal and can be approximated as [23]

$$\sigma_{noise} = \frac{v_{nyq}}{\sqrt{2N}\pi\beta}\sqrt{\left(1 + \frac{1}{SNR_{lin}}\right)^2 - \beta^2} \tag{26}$$

where $v_{nyq} = 40$ m/s is the Nyquist velocity, $N = 40$ is the number of pulses averaged across the 5-km integration length envisaged for the WIVERN radar, $\beta = 0.98\exp[-8((\pi\delta_v\ \ T_{hv})/\lambda)^2]$, $\delta_v = 3$ m/s is a characteristic broadening of the Doppler spectrum for the WIVERN mission (see [23]), $T_{hv} = 20\ \mu$s is the separation between the pulses that are used to derive the Doppler velocity [22], $\lambda = 3.2$ mm, and SNR_{lin} is the linear signal-to-noise ratio. Note that the error related to the phase shift estimate between different radar pulse pairs strongly increases when moving toward SNR=0 dB. Therefore, attenuation, which can be significant at W-band frequencies, increases noise (but not biases) in the Doppler signal.

Another potentially important source of error is pointing errors associated with either thermoelastic distortion of the antenna or uncertainties in attitude determination. Industrial studies [5] have demonstrated that the contribution of random pointing errors is limited to ≈ 0.5 ms^{-1}. Systematic errors, with periods longer than a day, introduce more significant wind

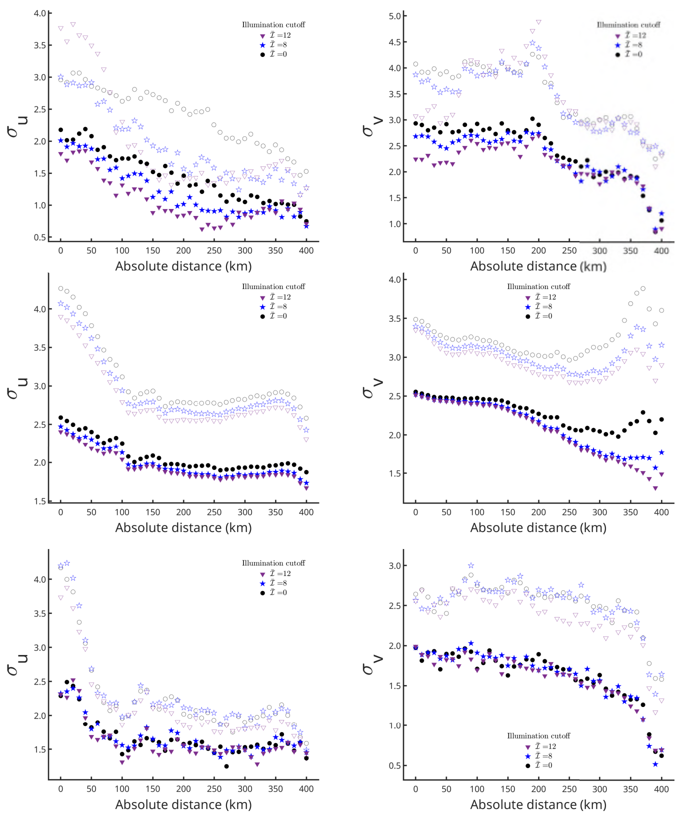

Fig. 13. Standard deviations of errors between reconstructed and true wind fields as a function of absolute distance from the satellite ground track for Area 1 (top), Area 2 (middle), and Area 3 (bottom). The left figure shows the standard deviation for the zonal wind component (σ_u), while the right figure displays the standard deviation for the meridional wind component (σ_v). Results are shown for different scene-averaged illumination cutoff thresholds: no cutoff (black circles), cutoff = 8 (blue stars), and cutoff = 14 (purple triangles). Filled markers represent cases without noise, while unfilled markers indicate cases with noise.

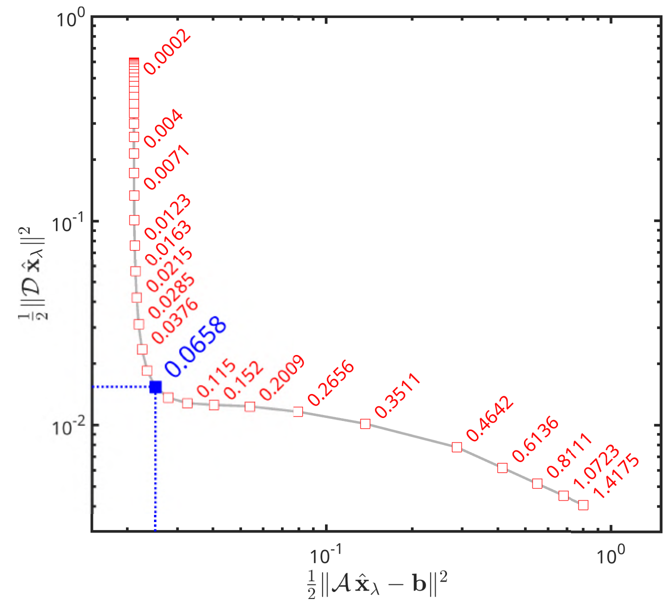

Fig. 14. L-curve used to select the regularization parameter λ. The curve shows the tradeoff between the data misfit, $1/2\|\mathcal{A}\hat{\mathbf{x}}_\lambda - \mathbf{b}\|_2^2$, and the regularization term, $1/2\|\mathcal{D}\hat{\mathbf{x}}_\lambda\|_2^2$, for different values of λ (red markers). We identify the optimal parameter at the corner of the curve, indicated by the blue marker, corresponding to $\hat{\lambda} = 0.0658$.

velocity errors that can be largely reduced through calibration techniques (e.g., using the altimeter technique and the surface zero-Doppler signature [5], [49], [50]).

Our methodology aims at retrieving the horizontal wind components at a spatial resolution of 10×10 km^2. In all experiments, the multiscale inversion is performed using a sequence of decreasing correlation lengths: $L = 40$, 20, 10, and 5 km. The illumination cutoff for the initial guess interpolation (see Section IV-A) is set to $\mathcal{I}_{\text{cutoff}} = 0.5$. The regularization parameter λ is selected at each step via the L-curve criterion, as illustrated for a representative case in the Appendix.

A. Case Studies

1) Hurricane Irma (Area 1): To demonstrate the effectiveness of the multiscale approach, we analyze the case study of Hurricane Irma [see Fig. 5 (left-center)], which caused widespread destruction in the Caribbean and the southeastern United States in 2017. Fig. 9 shows the cross section of the hurricane at an altitude of approximately 7 km, while Fig. 9(a) shows the reflectivity measured by the 94-GHz WIVERN radar. At this altitude, numerous targets exhibit reflectivity well above the WIVERN radar's sensitivity threshold (−18 dBZ), confirming the presence of strong scattering signals. This is confirmed by the illumination map [see Fig. 9(b)], which is computed according to (21) with $L = 40$ km. Darker regions (approaching black) indicate areas with sparse or absent sampling due to limited illumination, while lighter regions (approaching white) represent well-illuminated areas with densely collected samples.

Fig. 9(c) and (d) shows the model zonal (u) and meridional (v) winds, which serve as benchmarks for our wind retrieval case study. In these figures, the black dots represent radar-sampled points corresponding to the WIVERN scanning pattern, where the reflectivity exceeds the noise level of −18 dBZ, and no strong convection is present (i.e., $|w| \leq 2$ m/s). The characteristic dipole structure of both the meridional and zonal wind fields is evident, with maximum values on the order of 40–50 m/s. This structure is typical of cyclonic circulation.

The retrieval procedure described in Section IV is applied to the simulated WIVERN measurements; results corresponding to the different scales (L) are shown in Fig. 10 for the zonal (left column) and meridional (right column) winds. The first guess winds derived by using the inversion obtained from the solution of (20) (top) already show the hurricane dipole structure, but the fields are coarse because the methodology uses a correlation length $L = 25$ km. As the model undergoes further refinement by adopting shorter and shorter correlation lengths ($L = 10$ and $L = 5$ km, center and bottom figures), the resolution of the retrieved models and the errors in the retrieved fields improve progressively (from top to bottom). Note that, for the final iteration of the retrieval, the zonal winds are characterized by larger errors than the meridional ones and are mainly confined to the region close to the satellite ground track. This is expected because of the WIVERN observing geometry. Other large errors are present in areas with poor illumination (e.g., the top and bottom left corners).

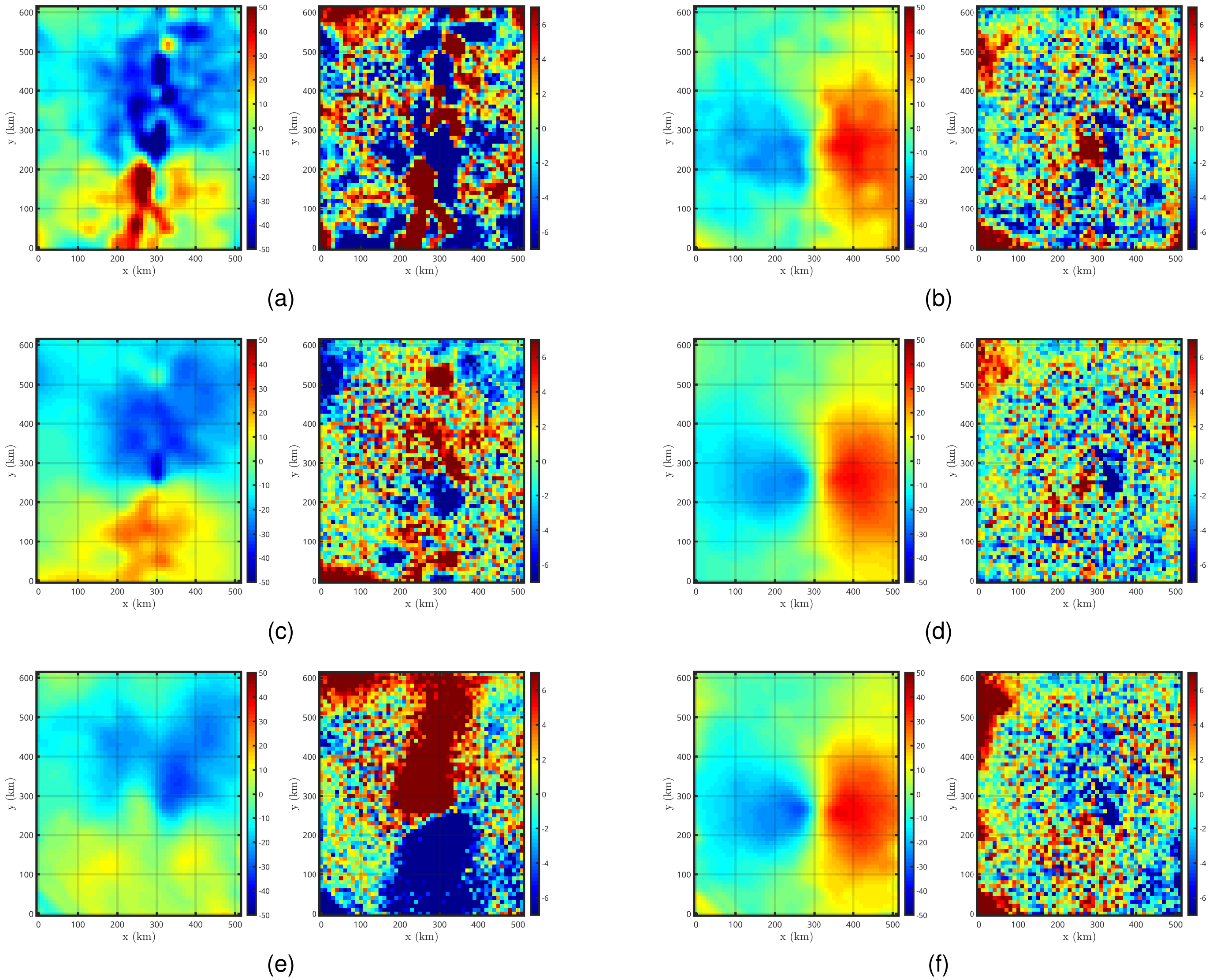

Fig. 15. Retrievals of the horizontal wind for the scene shown in Fig. 9 for the first guess of u and v, respectively, obtained from the solution of (20). The first column [(a)-(c)-(e)] illustrates results for the zonal wind (u), whereas the second column [(b)-(d)-(f)] shows the meridional wind (v). (a) and (b) Retrieved solution for the non-regularized case ($\lambda = 0$) with the corresponding errors computed with respect to the model reference fields depicted in Fig. 9(c) and (d). (c) and (d) Retrieved solution using the optimal λ-value ($\lambda = \hat{\lambda} = 0.0658$). (e) and (f) Retrieved models using $\lambda = 0.8111$.

2) Mid-Latitude Storm in the Southern Ocean (Area 2): The second example [see Fig. 5 (right center)] is an extensive cold front with strong winds in the Southern Ocean, as typically found in this region [51]. The 94-GHz WIVERN reflectivity [see Fig. 11(a)] follows the characteristic comma shape observed in these systems in geostationary visible images. The illumination map ($\mathcal{I}_L$) with $L = 40$ km [see Fig. 11(b)] highlights the absence of clouds in the western part with darker regions (approaching black) indicating areas with sparse or absent sampling.

Fig. 11(c) and (d) shows model zonal winds (u) blowing at more than 40 m/s eastward in the Northern part and at more than 25 m/s westward in the Southern part. Meridional (v) winds blow weakly northward in the upper and turn strongly southward in the center of the system.

Fig. 11(e) and (g) presents the final retrieved models after completing the multiscale processing, while Fig. 11(f) and (h) shows the corresponding errors computed with respect to the model reference fields. We notice that the illuminated areas are reconstructed very effectively, whereas areas without illumination are not reconstructed, as expected due to insufficient information. In addition, the regions between measurements are also satisfactorily reconstructed, thanks to the application of the multiscale approach. This is demonstrated in Fig. 11(f) and (h), which show a low error in the radar-illuminated region and its surrounding areas, as depicted by the predominance of the green color in these areas. Areas shaded correspond to regions where retrieval is performed, but it is inaccurate due to insufficient illumination ($\mathcal{I}_L^{(l)} < 0.5$).

3) Frontal System in the Atlantic Ocean Off Labrador (Area 3): As a final case study, we consider the passage of the WIVERN radar over a frontal system in the Atlantic Ocean near the Labrador region Fig. 5 (bottom), here referred to as Area 3. In particular, the analysis focuses on a cross section at 5-km altitude, with the 94-GHz reflectivity shown in Fig. 12(a). Also, this area has regions that are not very well illuminated, with no measurements for hundreds of km [(b)], as shown by the mean illumination ($\bar{\mathcal{I}}_L$) equal to 14.11. We use the zonal (u) and meridional (v) winds as References in the models shown in Fig. 12(c) and (d), respectively. In Fig. 12(e) and (g), we present the retrieved models, while, in Fig. 12(f) and (h), we show the corresponding errors relative to the reference fields in (c) and (d). As before, the results show that our multiscale approach yielded a satisfactory reconstruction of the wind fields in areas with decent radar illumination.

B. Statistical Analysis

To evaluate the characteristic errors in the retrievals of the u and v components, we simulated several WIVERN-like observations for various ascending and descending overpasses, with a zonal separation of 200 km, across the three systems depicted in Fig. 5 and described in Section III. For Area 1, we analyzed 477 scenes in total, comprising 19 ascending and 34 descending overpasses, with wind fields extracted at 9 different heights. For Area 2 (3), we examined 450 (160) scenes, comprising 16 (11) ascending and 29 (21) descending overpasses, with wind fields extracted for 10 (5) different heights.

Fig. 13 shows the errors (standard deviation of the difference between the retrieved and true models) associated with the reconstructed wind fields u (left) and v (right) compared to the reference models, for Area 1 (top), Area 2 (middle), and Area 3 (bottom). We calculated the errors as a function of the absolute distance between the positions where we recorded the measurements and the satellite ground track. Points with illumination $\mathcal{I}_L^{(l)} < 0.5$ have been excluded from the analysis. In addition, we evaluated the impact of scene illumination on these errors. For this purpose, we used the mean scene illumination value (22), $\bar{\mathcal{I}}$, as a cutoff parameter. In this regard, we considered three different cutoff values: $\bar{\mathcal{I}} = 12$ (downward purple triangles), $\bar{\mathcal{I}} = 8$ (blue stars), and $\bar{\mathcal{I}} = 0$ (black circles). In this figure, filled markers refer to the noise-free case, and unfilled markers refer to the results obtained in the presence of noise.

For both wind components, the reconstruction error decreases with increasing absolute distance, particularly within the first 200 km. This is caused by the sparser sampling and the lack of independent views in correspondence to the central part of the swath (see Fig. 4). Moreover, the pronounced reduction in errors for higher illumination cutoff values indicates that larger illumination cutoffs improve the accuracy of the retrieved wind fields. This effect is particularly evident for $\bar{\mathcal{I}} = 12$, where we consistently achieve the lowest errors. We also observe that noise significantly affects reconstruction, as errors in the noisy case (unfilled markers) remain consistently higher than those in the noise-free case (filled markers). In the left figure, corresponding to σ_u, we see a rapid decrease in error over the initial 100 km, followed by gradual stabilization. The lowest errors occur for $\bar{\mathcal{I}} = 12$, while $\bar{\mathcal{I}} = 8$ yields slightly higher values, and $\bar{\mathcal{I}} = 0$ results in the highest errors. A similar trend is present in σ_v (right figure) although the error stabilization appears to occur at slightly larger distances. These results demonstrate that the illumination cutoff significantly influences the quality of the reconstructed wind fields. Higher cutoff values lead to improved accuracy, while noise systematically increases errors. Our findings highlight the importance of optimizing the illumination cutoff when applying this reconstruction method in practical scenarios.

VI. Conclusion and Final Remarks

Progress in Earth observation technology suggests that the next generation of space-based atmospheric radars will be able to map mesoscale winds within cloud and precipitation systems. WIVERN, selected by ESA as the Earth Explorer 11 mission, proposes to measure in-cloud wind profiles using a conically scanning W-band Doppler radar. In this article, a gap-filling and reconstruction algorithm for the horizontal wind vector is proposed, based on WIVERN's ability to measure LoS winds in nearly overlapping volumes, almost simultaneously from different vantage points as the satellite moves rapidly over the observed scene. The algorithm starts with an initial wind field derived at coarse scales from an analytical solution and downscalers the wind field to finer scales. The results show that, for scenes having a healthy number of clouds, it is possible to reconstruct the zonal and meridional winds with uncertainties between 2 and 4 m/s depending on the illumination and the azimuthal diversity of the observed region. Accuracy is generally reduced in the central part of the swath, near the ground track, due to sparse sampling and a lack of independent views.

The algorithm reconstructs the horizontal wind field at each level independently. Future work should aim to reconstruct the full 3-D structure of the horizontal wind field, including its vertical correlation. A key assumption of the algorithm is that convective areas are screened out (i.e., horizontal winds are retrieved only where vertical motions can be neglected). Further studies will focus on assessing the potential of WIVERN observations to identify and quantify convective motions. In addition, the demonstrated tradeoff between spatial coverage and accuracy, revealed by illumination cutoff analysis, opens promising avenues for developing adaptive retrieval strategies optimized for future, specific studies. Another interesting avenue of research could be to retrieve wind features with strong small-scale variability (such as the winds in the inner cores of hurricanes) when observed with very dense sampling, as occurs in the last 20 km near the edge of the WIVERN swath.

Appendix: Impact of the Regularization Parameter

In this appendix, we illustrate the impact of the regularization parameter λ on the stability and physical consistency of the horizontal wind retrieval. The formulation of the regularized problem is described in Section IV-B. We focus on the Area 1 case study (Hurricane Irma), depicted in Section V-A1, as a representative example, noting that all other cases exhibit similar behavior.

We select λ objectively using the L-curve criterion [17], which balances data fidelity and enforcement of the mass-conservation constraint [17], [43], [44], [45]. Fig. 14 shows the resulting L-curve, constructed from the data misfit $1/2\|\mathcal{A}\hat{\mathbf{x}}_\lambda - \mathbf{b}\|_2^2$ and the regularization term $1/2\|\mathcal{D}\hat{\mathbf{x}}_\lambda\|_2^2$ for a range of λ values. We determine the optimal parameter as the point minimizing the distance to the origin of the L-curve using (24). In this case, we obtain $\hat{\lambda} = 0.0658$, corresponding to the corner of the curve.

Fig. 15 shows the practical consequences of the choice of λ by comparing retrieved horizontal wind fields obtained with three representative values. For $\lambda = 0$, the solution is dominated by small-scale noise and lacks physical coherence [(a) and (b)] when compared with the benchmark model (see Fig. 9), particularly in poorly sampled regions. Using the optimal value $\lambda = \hat{\lambda}$ yields a stable and physically consistent solution that preserves the main flow structures while suppressing nonphysical oscillations [(c) and (d)]. In contrast, excessively large values of λ produce overly smooth fields and attenuate dynamically relevant gradients [(e) and (f)].

The optimal value $\hat{\lambda}$, therefore, provides a robust compromise between numerical stability and physical realism and is adopted in the subsequent analyses.

References

[1] A. Stoffelen et al., "Wind profile satellite observation requirements and capabilities," *Bull. Amer. Meteorological Soc.*, vol. 101, no. 11, pp. E2005–E2021, 2020. [Online]. Available: https://journals.ametsoc.org/view/journals/bams/101/11/bamsD180202.xml

[2] O. Lux, M. Rennie, J. de Kloe, and O. Reitebuch, "Five years of Aeolus wind profiling: Global coverage and data quality," *EGUsphere*, vol. 2025, pp. 1–46, Oct. 2025. [Online]. Available: https://egusphere.copernicus.org/preprints/2025/egusphere-2025-4596/

[3] M. P. Rennie, L. Isaksen, F. Weiler, J. de Kloe, T. Kanitz, and O. Reitebuch, "The impact of Aeolus wind retrievals on ECMWF global weather forecasts," *Quart. J. Roy. Meteorological Soc.*, vol. 147, no. 740, pp. 3555–3586, Oct. 2021. [Online]. Available: https://rmets.onlinelibrary.wiley.com/doi/abs/10.1002/qj.4142

[4] S. Laroche and J. St-James, "Impact of the Aeolus level-2B horizontal line-of-sight winds in the environment and climate change Canada global forecast system," *Quart. J. Roy. Meteorological Soc.*, vol. 148, no. 745, pp. 2047–2062, Apr. 2022. [Online]. Available: https://rmets.onlinelibrary.wiley.com/doi/abs/10.1002/qj.4300

[5] "Report for mission selection: Earth explorer 11 candidate mission wivern," ESA WIVERN Team, European Space Agency (ESA), Noordwijk, The Netherlands, Tech. Rep. ESA-EOPSM-WIVE-RP-4798, 2025, doi: 10.5281/zenodo.15607041.

[6] A. J. Illingworth et al., "WIVERN: A new satellite concept to provide global in-cloud winds, precipitation, and cloud properties," *Bull. Amer. Meteorological Soc.*, vol. 99, no. 8, pp. 1669–1687, Aug. 2018, doi: 10.1175/bams-d-16-0047.1.

[7] A. Battaglia et al., "Peering inside tropical cyclones with the WIVERN space-borne Doppler radar," *Earth Space Sci.*, vol. 13, no. 3, p. 2025, 2026. [Online]. Available: https://agupubs.onlinelibrary.wiley.com/doi/abs/10.1029/2025EA004680

[8] N. Sasso et al., "Impact of WIVERN wind observations on ARPEGE numerical weather prediction model forecasts using an ensemble of data assimilation method," *Quart. J. Roy. Meteorological Soc.*, vol. 151, no. 770, p. 4991, Jul. 2025. [Online]. Available: https://rmets.onlinelibrary.wiley.com/doi/abs/10.1002/qj.4991

[9] S. Federico et al., "Assimilating WIVERN windpseudo-observations in WRF model: An application to the outstanding case of the medicane ianos," *Weather Climate Dyn.*, vol. 7, no. 1, pp. 165–183, Jan. 2026. [Online]. Available: https://wcd.copernicus.org/articles/7/165/2026/

[10] F. Tridon, A. Battaglia, A. Rizik, F. E. Scarsi, and A. Illingworth, "Filling the gap of wind observations inside tropical cyclones," *Earth Space Sci.*, vol. 10, no. 11, p. 2023, Nov. 2023. [Online]. Available: https://agupubs.onlinelibrary.wiley.com/doi/abs/10.1029/2023EA003099

[11] F. E. Scarsi, A. Battaglia, M. Maahn, and S. Lhermitte, "How to reduce sampling errors in spaceborne cloud radar-based snowfall estimates," *Cryosphere*, vol. 19, no. 10, pp. 4875–4892, Oct. 2025. [Online]. Available: https://tc.copernicus.org/articles/19/4875/2025/

[12] M. Coppola, A. Battaglia, F. Tridon, and P. Kollias, "Improved hydrometeor detection near the Earth's surface by a conically scanning spaceborne W-band radar," *Atmos. Meas. Techn.*, vol. 18, no. 19, pp. 5071–5085, Oct. 2025. [Online]. Available: https://amt.copernicus.org/articles/18/5071/2025/

[13] J. Gao, M. Xue, A. Shapiro, and K. K. Droegemeier, "A variational method for the analysis of three-dimensional wind fields from two Doppler radars," *Monthly Weather Rev.*, vol. 127, no. 9, pp. 2128–2142, Sep. 1999.

[14] S. R. Guimond, L. Tian, G. M. Heymsfield, and S. J. Frasier, "Wind retrieval algorithms for the IWRAP and HIWRAP airborne Doppler radars with applications to hurricanes," *J. Atmos. Ocean. Technol.*, vol. 31, no. 6, pp. 1189–1215, 2014.

[15] P. H. Hildebrand et al., "The ELDORA/ASTRAIA airborne Doppler weather radar: high-resolution observations from TOGA COARE," *Bull. Amer. Meteorological Soc.*, vol. 77, no. 2, pp. 213–232, Feb. 1996. [Online]. Available: https://journals.ametsoc.org/view/journals/bams/77/2/1520-0477_1996_077_0213_teadwr_2_0_co_2.xml

[16] C. López Carrillo and D. J. Raymond, "Retrieval of three-dimensional wind fields from Doppler radar data using an efficient two-step approach," *Atmos. Meas. Techn.*, vol. 4, no. 12, pp. 2717–2733, Dec. 2011. [Online]. Available: https://amt.copernicus.org/articles/4/2717/2011/

[17] P. C. Hansen, "Analysis of discrete ill-posed problems by means of the L-curve," *SIAM Rev.*, vol. 34, no. 4, pp. 561–580, Dec. 1992.

[18] C. Bunks, F. M. Saleck, S. Zaleski, and G. Chavent, "Multiscale seismic waveform inversion," *Geophysics*, vol. 60, no. 5, pp. 1457–1473, 1995.

[19] M. F. Khairoutdinov and D. A. Randall, "Cloud resolving modeling of the ARM summer 1997 IOP: Model formulation, results, uncertainties, and sensitivities," *J. Atmos. Sci.*, vol. 60, no. 4, pp. 607–625, Feb. 2003, doi: 10.1175/1520-0469(2003)060<0607:crmota>2.0.co;2.

[20] B. Stevens et al., "DYAMOND: The DYnamics of the atmospheric general circulation modeled on non-hydrostatic domains," *Prog. Earth Planet. Sci.*, vol. 6, no. 1, Dec. 2019, Art. no. 61, doi: 10.1186/s40645-019-0304-z.

[21] R. J. Doviak and D. S. Zrnić, *Doppler Radar and Weather Observations*. New York, NY, USA: Academic, 1993.

[22] A. Battaglia, A. Rizik, I. Sikaneta, and F. Tridon, "I and QS simulation and processing envisaged for spaceborne polarization diversity Doppler radars," *IEEE Trans. Geosci. Remote Sens.*, vol. 63, 2025, Art. no. 5101814.

[23] A. Battaglia et al., "Observation error analysis for the WInd VElocity radar nephoscope W-band Doppler conically scanning spaceborne radar via end-to-end simulations," *Atmos. Meas. Techn.*, vol. 15, no. 9, pp. 3011–3030, May 2022. [Online]. Available: https://amt.copernicus.org/articles/15/3011/2022/

[24] J. R. Holton, *An Introduction to Dynamic Meteorology*, 4th ed., New York, NY, USA: Academic, 2004.

[25] F. Mustich, A. Battaglia, F. Manconi, P. Kollias, and A. Parodi, "Convective–stratiform identification neural network (CONSTRAINN) for the WIVERN mission," *Remote Sens.*, vol. 17, no. 15, p. 2590, Jul. 2025. [Online]. Available: https://www.mdpi.com/2072-4292/17/15/2590

[26] A. Protat and C. R. Williams, "Assessment of CloudSat reflectivity measurements and ice cloud properties using ground-based and airborne cloud radar observations," *J. Appl. Meteorol. Climatol.*, vol. 50, pp. 2120–2138, Sep. 2011.

[27] H. Kalesse and P. Kollias, "Climatology of high cloud dynamics using profiling ARM Doppler radar observations," *J. Climate*, vol. 26, no. 17, pp. 6340–6359, Sep. 2013, doi: 10.1175/jcli-d-12-00695.1.

[28] K. Mroz, B. P. Treserras, A. Battaglia, P. Kollias, A. Tatarevic, and F. Tridon, "Cloud and precipitation microphysical retrievals from the EarthCARE cloud profiling radar: The C-CLD product," *EGUsphere*, vol. 2023, pp. 1–33, Jan. 2023. [Online]. Available: https://egusphere.copernicus.org/preprints/2023/egusphere-2023-56/

[29] P. Kollias, B. Puidgomènech Treserras, A. Battaglia, P. Borque, and A. Tatarevic, "Processing reflectivity and Doppler velocity from Earthcare's cloud profiling radar: The C-FMR, C-CD and C-APC products," *EGUsphere*, vol. 2022, pp. 1–25, 2022. [Online]. Available: https://egusphere.copernicus.org/preprints/2022/egusphere-2022-1284/

[30] K. Mróz, A. Battaglia, S. Kneifel, L. P. D'Adderio, and J. Dias Neto, "Triple-frequency Doppler retrieval of characteristic raindrop size," *Earth Space Sci.*, vol. 7, no. 3, p. 2019, Mar. 2020. [Online]. Available: https://agupubs.onlinelibrary.wiley.com/doi/abs/10.1029/2019EA000789

[31] K. Mróz, A. Battaglia, S. Kneifel, L. von Terzi, M. Karrer, and D. Ori, "Linking rain into ice microphysics across the melting layer in stratiform rain: A closure study," *Atmos. Meas. Techn.*, vol. 14, no. 1, pp. 511–529, Jan. 2021. [Online]. Available: https://amt.copernicus.org/articles/14/511/2021/

[32] E. J. Kendon et al., "Do convection-permitting regional climate models improve projections of future precipitation change?," *Bull. Amer. Meteorological Soc.*, vol. 98, no. 1, pp. 79–93, Jan. 2017. [Online]. Available: https://journals.ametsoc.org/view/journals/bams/98/1/bams-d-15-0004.1.xml

[33] S. Song, B. Beh, and R. K. Moore, "Scan patterns and accuracy of a radar wind sensor (RAWS)," Univ. Kansas Center Res., Inc., Lawrence, KS, USA, RSL Tech. Rep. 11170-2, 1995.

[34] C. Xue, Z. Ding, X. Shen, and X. Chen, "Three-dimensional wind field retrieved from dual-Doppler radar based on a variational method: Refinement of vertical velocity estimates," *Adv. Atmos. Sci.*, vol. 39, no. 1, pp. 145–160, Jan. 2022.

[35] J. Nocedal and S. J. Wright, *Numerical Optimization*. New York, NY, USA: Springer, 2006.

[36] J. V. T. D. Lima, S. L. E. F. D. Silva, J. M. D. Araújo, G. Corso, and G. Z. D. S. Lima, "Nonextensive statistical mechanics for robust physical parameter estimation: The role of entropic index," *Eur. Phys. J. Plus*, vol. 136, no. 3, p. 269, Mar. 2021.

[37] S. L. E. F. da Silva et al., "Refraction FWI of a circular shot OBN acquisition in the Brazilian presalt region," *IEEE Trans. Geosci. Remote Sens.*, vol. 62, 2024, Art. no. 5920518.

[38] A. Kirsch, *An Introduction to the Mathematical Theory of Inverse Problems*. Cham, Switzerland: Springer, 2021.

[39] J. C. A. Barata and M. S. Hussein, "The Moore–Penrose Pseudoinverse: A tutorial review of the theory," *Brazilian J. Phys.*, vol. 42, nos. 1–2, pp. 146–165, Apr. 2012.

[40] F. Preparata and M. Shamos, *Computational Geometry: An Introduction*. Cham, Switzerland: Springer, 2012.

[41] I. Amidror, "Scattered data interpolation methods for electronic imaging systems: A survey," *J. Electron. Imag.*, vol. 11, no. 2, pp. 157–176, Apr. 2002.

[42] T. A. Bobach, "Natural neighbor interpolation- critical assessment and new contributions, "Natural neighbor interpolation - critical assessment and new contributions," Ph.D. thesis, Fachbereich Informatik (Dept. Comput. Sci.), Technische Universität Kaiserslautern, Kaiserslautern, Germany, 2009. [Online]. Available: https://nbn-resolving.de/urn: nbn: de: hbz:386-kluedo-23517

[43] B. Borchers, C. H. Thurber, and R. Aster, *Parameter Estimation and Inverse Problems*, 3rd ed., Amsterdam, The Netherlands: Elsevier, 2018.

[44] H. W. Engl and W. Grever, "Using the L-curve for determining optimal regularization parameters," *Numerische Math.*, vol. 69, no. 1, pp. 25–31, Nov. 1994.

[45] R. Moustafa and A. S. Hadi, "Estimating the number of clusters in multivariate data by various fittings of the L-curve," *Comput. Appl. Math.*, vol. 44, no. 1, p. 39, Feb. 2025.

[46] T. Regińska, "A regularization parameter in discrete ill-posed problems," *SIAM J. Sci. Comput.*, vol. 17, no. 3, pp. 740–749, May 1996.

[47] W. A. Barbosa, S. L. E. F. da Silva, E. de la Barra, and J. M. de Araújo, "Full-waveform inversion based on generalized Rényi entropy using patched Green's function techniques," *PLoS ONE*, vol. 17, no. 11, pp. 1–27.

[48] A. Battaglia, R. Rabino, K. Mroz, F. Tridon, and A. Parodi, "Nonuniform beamfilling correction for the Doppler velocity measured by the WIVERN conically scanning radar," *J. Atmos. Ocean. Technol.*, vol. 43, no. 6, pp. 733–744, Jun. 2026. [Online]. Available: https://journals.ametsoc.org/view/journals/atot/aop/JTECH-D-25-0050.1/JTECH-D-25-0050.1.xml

[49] B. P. Treserras, P. Kollias, A. Battaglia, S. Tanelli, and H. Nakatsuka, "EarthCARE's cloud profiling radar antenna pointing correction using surface Doppler measurements," *Atmos. Meas. Techn.*, vol. 18, no. 20, pp. 5607–5618, Oct. 2025. [Online]. Available: https://amt.copernicus.org/articles/18/5607/2025/

[50] F. E. Scarsi, A. Battaglia, F. Tridon, P. Martire, R. Dhillon, and A. Illingworth, "Mispointing characterization and Doppler velocity correction for the conically scanning WIVERN Doppler radar," *Atmos. Meas. Techn.*, vol. 17, no. 2, pp. 499–514, Jan. 2024. [Online]. Available: https://amt.copernicus.org/articles/17/499/2024/

[51] L. G. Bennetts et al., "Closing the loops on Southern Ocean dynamics: From the circumpolar current to ice shelves and from bottom mixing to surface waves," *Rev. Geophys.*, vol. 62, no. 3, p. 2022, Sep. 2024.

Open Access funding provided by 'Politecnico di Torino' within the CRUI CARE Agreement